

Simultaneous three-dimensional variational assimilation of surface fine particulate matter and MODIS aerosol optical depth

Craig S. Schwartz,¹ Zhiqian Liu,¹ Hui-Chuan Lin,¹ and Stuart A. McKeen^{2,3}

Received 21 December 2011; revised 1 May 2012; accepted 3 May 2012; published 3 July 2012.

[1] Total 550 nm aerosol optical depth (AOD) retrievals from Moderate Resolution Imaging Spectroradiometer (MODIS) sensors and surface fine particulate matter (PM_{2.5}) observations were assimilated with the National Centers for Environmental Prediction (NCEP) Gridpoint Statistical Interpolation (GSI) three-dimensional variational (3DVAR) data assimilation (DA) system. Parallel experiments assimilated AOD and surface PM_{2.5} observations both individually and simultaneously. New 3DVAR aerosol analyses were produced every 6 h between 0000 UTC 01 June and 1800 UTC 14 July 2010 over a domain encompassing the continental United States. The analyses initialized Weather Research and Forecasting-Chemistry (WRF-Chem) model forecasts. Assimilating AOD, either alone or in conjunction with PM_{2.5} observations, produced better AOD forecasts than a control experiment that did not perform DA. Additionally, individual assimilation of both AOD and PM_{2.5} improved surface PM_{2.5} forecasts compared to when no DA occurred. However, the best PM_{2.5} forecasts were produced when both AOD and PM_{2.5} were assimilated. Considering the goodness of both AOD and PM_{2.5} forecasts, the results unequivocally show that concurrent DA of PM_{2.5} and AOD observations produced the best overall forecasts, illustrating how simultaneous DA of different aerosol observations can work synergistically to improve aerosol forecasts.

Citation: Schwartz, C. S., Z. Liu, H.-C. Lin, and S. A. McKeen (2012), Simultaneous three-dimensional variational assimilation of surface fine particulate matter and MODIS aerosol optical depth, *J. Geophys. Res.*, *117*, D13202, doi:10.1029/2011JD017383.

1. Introduction

[2] While considerable effort over recent years has focused on quantifying aerosol properties, transport, and distribution from numerical perspectives, aerosol modeling remains challenging given large uncertainties related to aerosol emission and interaction with nonlinear physical processes (e.g., radiative effects, cloud and precipitation formation). Further improvement of aerosol models is needed to better predict aerosol-related impacts to regional air quality, human health [Pope *et al.*, 2002], and climate change [Forster *et al.*, 2007]. Moreover, better specification of aerosol climatologies can improve numerical weather prediction (NWP) model forecasts of wind and precipitation [Rodwell, 2005].

[3] One method to improve model forecasts of aerosols is data assimilation (DA), which combines observations with numerical model output and can reduce uncertainties of initial aerosol fields. There are many DA methods, including

optimal interpolation (OI) [Lorenc, 1981], 3-dimensional variational (3DVAR) [Lorenc, 1986; Parrish and Derber, 1992; Rabier *et al.*, 1998], and 4-dimensional variational (4DVAR) [e.g., Huang *et al.*, 2009] algorithms, as well as several flavors of ensemble DA (EnDA) techniques, such as the ensemble Kalman filter (EnKF) [Evensen, 1994]. Although the specifics of these DA methods differ substantially, all produce a statistically optimal “analysis” that can initialize a NWP model forecast. Generally, a better representation of initial conditions (ICs) leads to better forecasts.

[4] Meteorological DA has been used for decades in most operational NWP centers to initialize their forecast models [e.g., Parrish and Derber, 1992; Lorenc *et al.*, 2000; Rabier *et al.*, 2000; Gauthier *et al.*, 2007]. However, aerosol DA remains in its infancy, with serious attempts only beginning in the 2000s. Since then, several studies have employed various algorithms to assimilate aerosol-related observations from satellites, due to their high spatiotemporal resolution and broad geographic coverage. For example, aerosol optical depth (AOD) measurements taken from various satellites were assimilated using OI [e.g., Collins *et al.*, 2001; Yu *et al.*, 2003; Generoso *et al.*, 2007; Adhikary *et al.*, 2008], Newtonian-nudging [Wang *et al.*, 2004], 2-dimensional variational (2DVAR) [Zhang *et al.*, 2008; Schroedter-Homscheidt *et al.*, 2010], 3DVAR [Liu *et al.*, 2011], and 4DVAR [Benedetti *et al.*, 2009] DA techniques. Furthermore, geostationary satellite dust loading retrievals were assimilated using 3DVAR [Niu *et al.*, 2008], and Sekiyama *et al.* [2010,

¹National Center for Atmospheric Research, Boulder, Colorado, USA.

²Cooperative Institute for Research in Environmental Sciences, University of Colorado Boulder, Boulder, Colorado, USA.

³Chemical Science Division, ESRL, National Oceanic and Atmospheric Administration, Boulder, Colorado, USA.

Corresponding author: C. Schwartz, National Center for Atmospheric Research, 3090 Center Green Dr., Boulder, CO 80301, USA. (schwartz@ucar.edu)

©2012. American Geophysical Union. All Rights Reserved. 0148-0227/12/2011JD017383

2011] used an EnKF to assimilate backscattering coefficients and depolarization ratios from the Cloud-Aerosol Lidar with Orthogonal Polarization (CALIOP) sensor onboard the Cloud-Aerosol Lidar and Infrared Pathfinder Satellite Observations (CALIPSO) satellite [Winker *et al.*, 2009]. These studies all noted that aerosol DA yielded improved model representations of initial and future aerosol fields.

[5] In addition to DA of satellite-derived aerosol data, observations from ground-based aerosol monitoring networks [Holben *et al.*, 1998; Welton and Campbell, 2002; Amiridis *et al.*, 2005], while limited in their areal coverage, have also been assimilated. For instance, surface measurements of total column AOD provided by the AEROSOL RObotic NETwork (AERONET) [Holben *et al.*, 1998] were assimilated with a global EnKF [Schutgens *et al.*, 2010]. Also, Kahnert [2008] used 3DVAR to assimilate a profile of surface-borne lidar backscattering coefficients. Additionally, Tombette *et al.* [2009] assimilated surface PM₁₀ (particulate matter with diameter <10 μm) observations over Europe using the OI method and Lin *et al.* [2008] assimilated PM₁₀ over China with an EnKF. Furthermore, Pagowski *et al.* [2010] assimilated surface PM_{2.5} (particulate matter with diameter <2.5 μm) observations over the United States using a 3DVAR approach and noted improved aerosol forecasts.

[6] Despite successful assimilation of aerosol-related observations from both ground and satellite platforms, to our knowledge, satellite and surface aerosol measurements have not yet been assimilated simultaneously. We surmise that concurrent assimilation of both satellite and surface aerosol observations should work synergistically to provide better overall aerosol forecasts than assimilating observations from just one source. This study tests this hypothesis by assimilating both surface PM_{2.5} observations from the United States Environmental Protection Agency (EPA) AIRNow network (<http://airnow.gov>) and total AOD retrievals at 550 nm from Moderate Resolution Imaging Spectroradiometer (MODIS) [Remer *et al.*, 2005] sensors onboard the Terra and Aqua satellites for a ~1.5 month long period over the continental United States (CONUS). Surface PM_{2.5} assimilation capability was added into the aerosol DA framework developed by Liu *et al.* [2011, hereinafter LIU11], who implemented AOD DA within the National Centers for Environmental Prediction (NCEP) Gridpoint Statistical Interpolation (GSI) 3DVAR DA system [Wu *et al.*, 2002; Kleist *et al.*, 2009] coupled to the Goddard Chemistry Aerosol Radiation and Transport (GOCART) aerosol scheme [Chin *et al.*, 2000, 2002; Ginoux *et al.*, 2001] within the Weather Research and Forecasting-Chemistry (WRF-Chem) model [Grell *et al.*, 2005]. LIU11 demonstrated the practical implementation of their system by assimilating MODIS AOD retrievals over a week-long period while studying a dust storm in East Asia, noting improved aerosol forecasts from AOD DA.

[7] This work builds upon LIU11 and serves several purposes. First, this study provides another look at AOD DA within the GSI/GOCART/WRF-Chem framework, but over a substantially longer period and different geographic region. Second, we describe and implement surface PM_{2.5} DA capability within LIU11's 3DVAR system. Finally, we simultaneously assimilate both AOD and surface PM_{2.5} observations, marking the first time both satellite and surface observations of aerosols have been simultaneously assimilated within a common framework.

[8] The next section briefly describes the modeling and DA systems, while section 3 describes the observation operators that linked the model fields to the PM_{2.5} and AOD observations. Section 4 details the observation sources and uncertainty. The experimental design is presented in section 5 and the results in section 6. A discussion of the results follows in section 7 before concluding in section 8.

2. Modeling and DA Systems

[9] The modeling and DA systems used here were described by LIU11. Therefore, generally brief descriptions follow, and important differences from LIU11 are noted.

2.1. WRF-Chem Model Configurations

[10] Version 3.3 of the WRF-Chem model was used to predict the transport of aerosols. WRF-Chem is an "online" model, as chemical and meteorological components are fully coupled. Aerosol direct and indirect effects through interaction with radiation, photolysis, and microphysical processes are allowed for certain combinations of aerosol and physical options.

[11] The GOCART was chosen as the aerosol option within WRF-Chem. While LIU11 coupled GOCART to the Regional Atmospheric Chemistry Mechanism (RACM) [Stockwell *et al.*, 1997] for gaseous chemistry, gaseous chemical transport was not simulated in this study. The GOCART model simulates several tropospheric aerosol types, including sulfate, dust, organic carbon (OC), black carbon (BC), and sea salt. For OC and BC, hydrophobic and hydrophilic components are considered. Many processes regarding the aerosol species' evolution are represented, including emission, advection, convection, diffusion, dry deposition, and wet deposition, as well as chemical reactions using prescribed OH, H₂O₂, and NO₃ fields for SO₂ and DMS oxidations [Chin *et al.*, 2002]. When GOCART is chosen as the aerosol module within WRF-Chem, forecasts of 3D mass mixing ratios of 14 aerosol species are produced: hydrophobic and hydrophilic OC and BC; sulfate; sea-salt in four particle-size bins (effective radii of 0.3, 1.0, 3.25, and 7.5 μm for dry air); and dust particles in five particle-size bins (effective radii of 0.5, 1.4, 2.4, 4.5, and 8.0 μm). Additionally, mixing ratio of a 15th variable representing unspiciated aerosol contributions to PM_{2.5} (hereafter, denoted as *P*) is also produced when GOCART runs within WRF-Chem, although *P* was not originally included in GOCART.

[12] While LIU11 examined simulations over Eastern Asia, this study focuses on aerosol analyses and WRF-Chem forecasts over the CONUS (Figure 1). The horizontal grid spacing was 20-km, there were 41 vertical levels, and the model-top was 50 hPa. A full suite of physical parameterizations [see Skamarock *et al.*, 2008, and references therein] were employed in WRF-Chem, including the Yonsei University (YSU) planetary boundary layer (PBL) scheme; WRF single-moment 5-class (WSM5) microphysics scheme; Rapid Radiative Transfer Model (RRTM) longwave and Goddard shortwave radiation schemes; Noah land surface model; and Grell-3D cumulus parameterization. Lateral boundary conditions (LBCs) for meteorological fields were provided by the NCEP North American Mesoscale (NAM) [Rogers *et al.*, 2009] model at 20-km horizontal grid spacing.

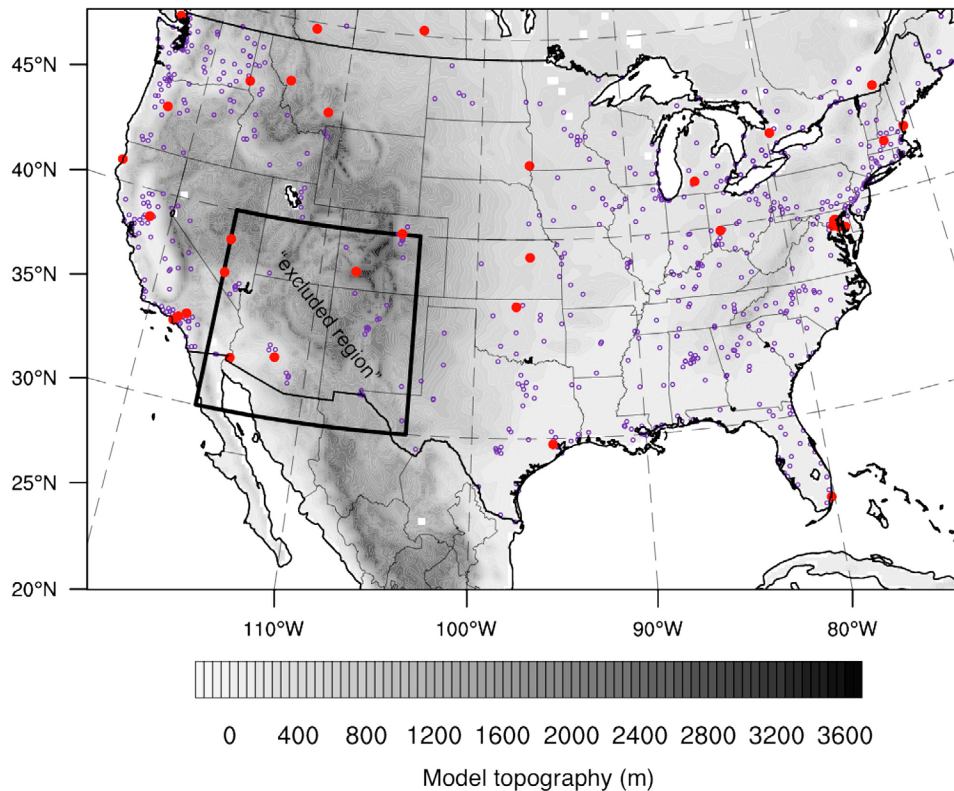


Figure 1. Computational domain overlaid with model topography (m). Small open circles depict locations of AIRNow sites used for PM_{2.5} assimilation and large filled dots indicate AERONET sites used for AOD verification. The AIRNow sites were also used to verify PM_{2.5} forecasts, except verification did not occur at the AIRNow sites within the boxed region, referred to as the “excluded region” (see section 6.2.1).

[13] Aerosol LBCs represented clean oceanic conditions. Mixing ratios at the lateral boundaries of the 14 speciated WRF-Chem/GOCART aerosol variables were assigned near zero values, while boundary values for the unspiciated contributions to PM_{2.5} (P) equaled 1.0 $\mu\text{g}/\text{kg}$ below 1-km and decreased exponentially with height to 0.1 $\mu\text{g}/\text{kg}$ at the model top. Anthropogenic emissions of SO₂, primary PM_{2.5}, and hydrophobic OC and BC were based on the weekday U. S. EPA NEI-2005 emissions inventory [U.S. Environmental Protection Agency, 2010]. The gridded (4-km resolution) and point source hourly emission files used here are available at <ftp://aftp.fsl.noaa.gov/divisions/taq/emissions> data. More details and evaluations of the inventory are found in Kim *et al.* [2011]. Emissions of dust and sea-salt were parameterized within the GOCART model [Chin *et al.*, 2002].

[14] The aerosol DA system is now described.

2.2. GSI 3DVAR DA System

[15] NCEP’s GSI 3DVAR DA system was used to assimilate both AOD and surface PM_{2.5} observations. A 3DVAR system calculates a best fit “analysis” considering two sources of initial information: observations at irregularly spaced points and a gridded background (or “first-guess”) field, typically taken from a short-term model forecast. Associated with the background and observations are their error characteristics. Given the background, observations, and errors, the analysis vector (\mathbf{x}) can be determined by

minimizing a scalar cost-function $J(\mathbf{x})$ given by

$$J(\mathbf{x}) = \frac{1}{2}(\mathbf{x} - \mathbf{x}_b)^T \mathbf{B}^{-1}(\mathbf{x} - \mathbf{x}_b) + \frac{1}{2}[\mathbf{H}(\mathbf{x}) - \mathbf{y}]^T \mathbf{R}^{-1}[\mathbf{H}(\mathbf{x}) - \mathbf{y}], \quad (1)$$

where \mathbf{x}_b denotes the background vector, \mathbf{y} is a vector of observations, and \mathbf{B} and \mathbf{R} represent the background and observation error covariance matrices, respectively. The covariance matrices determine how closely the analysis is weighted toward the background and observations. H is the potentially nonlinear “observation operator” that interpolates model grid point values to observation locations and transforms model-predicted variables to observed quantities.

[16] Both the background and analysis are vectors comprised of “analysis variables” (or “control variables”). While a model might predict tens or even hundreds of prognostic variables, only the analysis variables are updated during DA. For meteorological assimilation the analysis variables typically are 3D wind, temperature, and moisture fields. However, here, the analysis variables were the 3D mass mixing ratios of the 15 WRF-Chem/GOCART aerosol variables at each grid point. This choice of variables was similar to LIU11, but LIU11 analyzed just the 14 speciated WRF-Chem/GOCART variables and did not include P as a control variable. P was introduced into the analysis vector here as it is an important contributor to PM_{2.5}. This speciated approach to aerosol DA within a variational system was a

novel development introduced by LIU11. By using individual aerosol species as control variables, no assumptions were made regarding the contribution of each species' mass to the total aerosol mass or shapes of the vertical profiles, unlike many previous studies [e.g., Zhang *et al.*, 2008; Benedetti *et al.*, 2009; Pagowski *et al.*, 2010] that employed total AOD or total aerosol mass as control variables (see LIU11 for a discussion). Thus, while Pagowski *et al.* [2010] also assimilated surface PM_{2.5} observations with GSI, their system fundamentally differed from ours, due to their choice of PM_{2.5} as the control variable.

[17] The 3DVAR algorithm requires background error covariance (BEC) statistics for each analysis variable. GSI uses recursive filters and permits spatially inhomogeneous BECs [Wu *et al.*, 2002]. Only standard deviation and horizontal and vertical length-scales of the background error are needed to apply recursive filters both horizontally and vertically. The BECs were computed for each aerosol species as in LIU11 by utilizing the "NMC method" [Parrish and Derber, 1992]. This method calculates BECs by taking differences between forecasts of different lengths valid at common times. Differences of 24- and 12-h WRF-Chem forecasts of the analysis variables valid at the same time for 57 pairs at either 0000 and 1200 UTC over July 2008 were used to compute the aerosol BECs. No cross-correlation between the different species was considered, as GSI 3DVAR cannot directly model the cross-correlations. Multivariate correlations among the aerosol species could be more easily achieved using an EnDA technique.

[18] Since only total 550 nm AOD and surface PM_{2.5} observations were assimilated to analyze the 3D mass mixing ratios of 15 aerosol variables, the 3DVAR problem was under-constrained in terms of observational information content, and AOD and PM_{2.5} DA may not improve analyses and forecasts of individual species. However, the problem was well constrained mathematically due to use of prior information from the model background. Given the lack of vertical information provided by the observations, distribution of the analysis increments (difference between the analysis and background) onto the different species was mostly model-driven, with the observation and background error covariances acting as the main constraints.

[19] The 15 analysis variables were also used to compute model-simulated values of AOD and PM_{2.5}, as the next section details.

3. Observation Operators

[20] To assimilate any observation with a 3DVAR system, a model estimate of the observation is required. The observation operator (or "forward operator") performs this task using model variables. Model simulated PM_{2.5} and AOD observations were calculated from the 3D fields of the 15 aerosol control variables and the density of dry air (ρ_d). The analysis variables and ρ_d were bilinearly interpolated to the observation locations before the formulas were applied. The Jacobians of the forward operators were also found and used to distribute the AOD and PM_{2.5} increments back onto the speciated 3D aerosol profiles in the 3DVAR minimization process.

[21] The forward operators are now described.

3.1. P.M_{2.5} Forward Operator

[22] Model-simulated PM_{2.5} observations (Π_m) were computed by summing weighted mass mixing ratios of fine aerosol particles, given as

$$\Pi_m = \rho_d [P + D_1 + 0.286D_2 + 1.8(O_1 + O_2) + B_1 + B_2 + S_1 + 0.942S_2 + 1.375U], \quad (2)$$

where P represents unspiciated aerosol contributions to PM_{2.5}; U denotes sulfate; O_1 and O_2 (B_1 and B_2) are hydrophobic and hydrophilic OC (BC), respectively; and D_1 and D_2 (S_1 and S_2) are dust (sea salt) aerosols in the smallest and 2nd smallest size bins. This formula is identical to the one used in WRF-Chem to diagnose PM_{2.5} from the GOCART aerosol module. Coefficients <1 in equation (2) account for overlap of GOCART dust and sea-salt size bins with the 2.5 μm diameter cutoff for PM_{2.5}. Coefficients >1 in equation (2) empirically account for additional fine particulate mass not predicted explicitly by GOCART, such as oxygen contained in organic aerosols (associated with OC) and ammonium (typically associated with sulfate aerosols). The coefficients of the aerosol species inside the brackets of equation (2) assume aerosol mixing ratios of $\mu\text{g}/\text{kg}$, so multiplication by ρ_d was required to convert the units to $\mu\text{g}/\text{m}^3$ for consistency with the observations. While equation (2) was valid for all model levels, it was only applied within GSI at the lowest vertical level, since just surface PM_{2.5} observations were assimilated.

3.2. AOD Forward Operator

[23] LIU11 thoroughly described the AOD observation operator, and, thus, only a brief explanation follows. The community radiative transfer model (CRTM) [Han *et al.*, 2006; Liu and Weng, 2006] was coupled to GSI and computed model-simulated AOD at MODIS and AERONET wavelengths using the profiles of the 14 speciated WRF-Chem/GOCART aerosol variables. Although the CRTM does not explicitly include P in its formulation of AOD, we assumed P had optical properties similar to D_1 and D_2 and added 78% of P to D_1 and 22% of P to D_2 before calculating AOD. This approach differed from LIU11—who did not include P in the AOD calculation—and seemed to improve assimilation statistics without producing any adverse effects. As in LIU11, external aerosol mixtures were assumed.

[24] The CRTM computes the effective radii (r_{eff}) of the 14 speciated WRF-Chem/GOCART aerosol variables assuming spherical aerosol particles and lognormal size distributions. The refractive index was also computed for each species, considering hygroscopic growth for sea salt, sulfate, and hydrophilic OC and BC. Using the size distribution and refractive index, Mie scattering code [van de Hulst, 1957] was applied to compute the mass extinction coefficient α (m^2/g) for each aerosol type at a wavelength λ . Then, AOD for the i th aerosol type (i.e., for each of the 14 speciated WRF-Chem/GOCART variables) at the j th model layer (τ_{ij}) for a particular λ was calculated as

$$\tau_{ij}(\lambda) = \alpha(\lambda, i, r_{eff}) \times c_{ij}, \quad (3)$$

where c_{ij} is the aerosol layer mass in g/m^2 . The final step involves summing equation (3) over the 14 speciated WRF-

Chem/GOCART aerosol variables ($i=1, 2, \dots, 14$) and the k discretized model levels to compute the model-simulated column total AOD (τ_m):

$$\tau_m(\lambda) = \sum_{j=1}^k \sum_{i=1}^{14} \tau_{ij}(\lambda). \quad (4)$$

4. Observations Sources and Errors

[25] This study considers the assimilation of both surface PM_{2.5} and MODIS AOD observations. The observations and their associated errors are now described.

4.1. Surface PM_{2.5} Observations

[26] PM_{2.5} observations from the EPA AIRNow network were assimilated, similar to *Pagowski et al.* [2010]. AIRNow provides hourly averaged surface PM_{2.5} concentrations at many sites over the USA and Canada. Data are available continuously in near-real time. Figure 1 shows the locations of AIRNow sites whose data were assimilated. Observing sites spanned most of the domain but were primarily located in urban and suburban areas.

[27] The total uncertainty associated with a PM_{2.5} observation included contributions from measurement and representation errors. *Pagowski et al.* [2010] used a measurement error (ϵ_o) of 2 $\mu\text{g}/\text{m}^3$. However, here, to associate higher PM_{2.5} values with larger measurement errors, ϵ_o was defined as $\epsilon_o = 1.5 + 0.0075 \cdot \Pi_o$, where Π_o denotes an AIRNow PM_{2.5} observation and the units of each term are $\mu\text{g}/\text{m}^3$.

[28] Representativeness errors arise due to inaccuracies in the forward operator and interpolation from the model grid to the observation location. Following *Elbern et al.* [2007] and *Pagowski et al.* [2010], the representativeness error (ϵ_r) was calculated as

$$\epsilon_r = \gamma \epsilon_o \sqrt{\frac{\Delta x}{L}}, \quad (5)$$

where γ is an adjustable parameter scaling ϵ_o ($\gamma = 0.5$ was used), Δx is the grid spacing (here, 20-km), and L is the radius of influence of an observation and was set to 2-, 4-, and 10-km for urban, suburban, and rural AIRNow sites, respectively. The total PM_{2.5} error ($\epsilon_{PM2.5}$) was defined as

$$\epsilon_{PM2.5} = \sqrt{\epsilon_o^2 + \epsilon_r^2}, \quad (6)$$

which constituted the diagonal elements in the \mathbf{R} matrix (equation (1)) for PM_{2.5} observations. Additionally, the PM_{2.5} observations were subject to quality control (QC). PM_{2.5} values $>200 \mu\text{g}/\text{m}^3$ were deemed unrealistic and not assimilated, and observations leading to innovations (observations minus the model-simulated observations determined from the first-guess field) exceeding 100 $\mu\text{g}/\text{m}^3$ were also omitted.

4.2. MODIS AOD Retrievals

[29] As in LIU11, level 2 AOD retrievals over land and sea from MODIS sensors on the Terra and Aqua satellites were assimilated. Only the dark target product [*Remer et al.*, 2005], available from both satellites, was assimilated. MODIS retrieved AOD was provided at 470, 550, 660, 870,

1240, 1630, and 2130 nm wavelengths, but only AOD at 550 nm was assimilated in this study. The original MODIS AOD level 2 products are at 10- \times 10-km resolution but the AOD retrievals were thinned to a 60-km grid. Satellite observations are commonly thinned to scales coarser than the model grid to reduce data volume and correlations between errors of adjacent observations, which are not considered in the observation error covariance matrix [*Liu and Rabier*, 2002].

[30] Over the domain (Figure 1), MODIS AOD products provided coverage primarily around 1800 UTC (day time), with some coverage near 0000 UTC. Figure 2a shows the available dark-target AOD retrievals from both satellites between 1500 and 2100 UTC 17 June. During this time-frame, AOD retrievals were generally available throughout the entire domain but the specific coverage varied. Around 0000 UTC, Aqua provided observations west of ~ 105 -degrees longitude on some days (Figure 2b), but observations from Terra were unavailable.

[31] The total observation error for AOD (ϵ_{AOD}) followed *Remer et al.* [2005] and depended on whether the MODIS AOD observation (τ_o) was taken over water or land:

$$\epsilon_{AOD} = \begin{cases} 0.03 + 0.05\tau_o & \text{points over water} \\ 0.05 + 0.15\tau_o & \text{points over land} \end{cases}. \quad (7)$$

[32] Only AOD retrievals marked with the best MODIS QC flag were assimilated.

5. Experimental Design

[33] Four parallel experiments were designed to evaluate the impact of MODIS AOD and surface PM_{2.5} DA on aerosol analyses and forecasts over the CONUS. One experiment (“noDA”) served as the control and did not employ any DA. The other three experiments all performed 3DVAR DA but assimilated different observations. Just MODIS AOD data were assimilated by one experiment (“AOD”), while another solely assimilated surface PM_{2.5} observations (“PM_{2.5}”). The final experiment assimilated both surface PM_{2.5} and AOD observations (“AOD+PM_{2.5}”). The experiments were all run over the same domain (Figure 1) and used identical WRF-Chem settings and physical parameterizations as described in section 2.1.

[34] As the AIRNow network provides hourly averaged PM_{2.5} observations, they were assigned “effective” valid times of 30 min past each hour. PM_{2.5} observations with effective times within 1-h of the analysis times were assimilated (i.e., a 1200 UTC analysis assimilated PM_{2.5} observations with effective valid times of 1130 and 1230 UTC), while AOD observations within 3 h of the analysis times were eligible for assimilation. Given the Aqua and Terra satellite coverages, AOD was primarily assimilated during 1800 UTC analyses, but a few observations were assimilated at 0000 UTC. Due to lack of coverage, 550 nm MODIS AOD was not assimilated in 0600 or 1200 UTC analyses.

[35] The four experiments all began from the same set of ICs valid 0000 UTC 01 June 2010 that were spun-up over 5 days beginning 0000 UTC 27 May from initial aerosol fields equivalent to the aerosol LBCs to permit the adjustment of the aerosol concentrations, similar to *Pagowski et al.* [2010]. All experiments initialized a new WRF-Chem

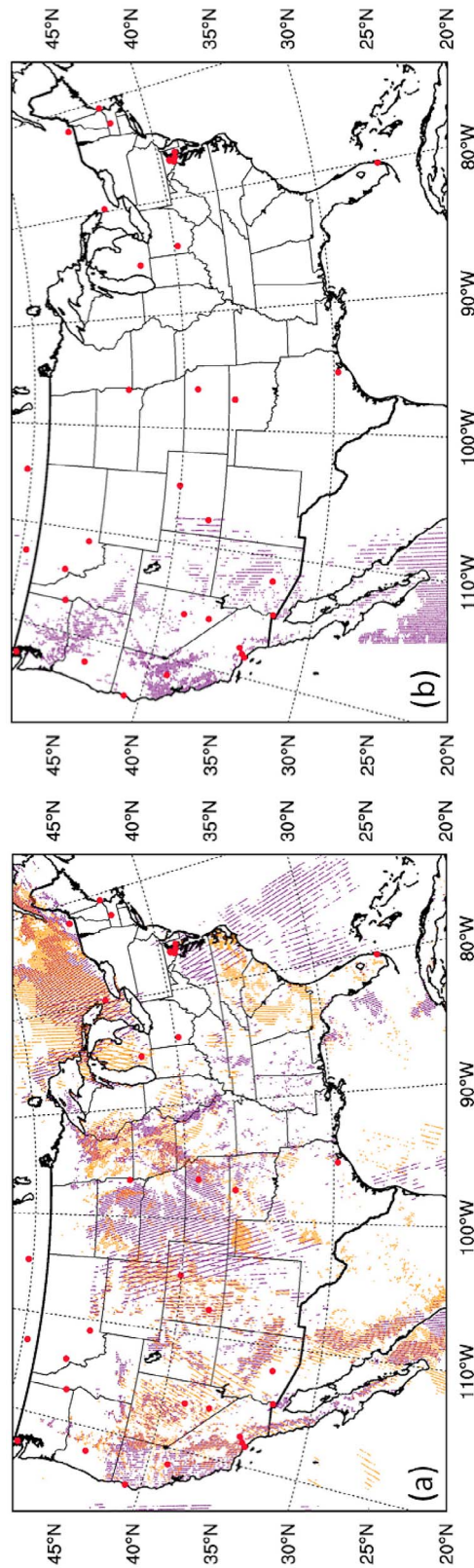


Figure 2. The 550 nm MODIS AOD coverage from the Aqua and Terra satellites between (a) 1500–2100 UTC 17 June and (b) 2100 UTC 22 June to 0300 UTC 23 June. Dark-surface retrievals from Aqua (Terra) are shown in purple (gold). As in Figure 1, large filled dots indicate AERONET sites used for AOD verification.

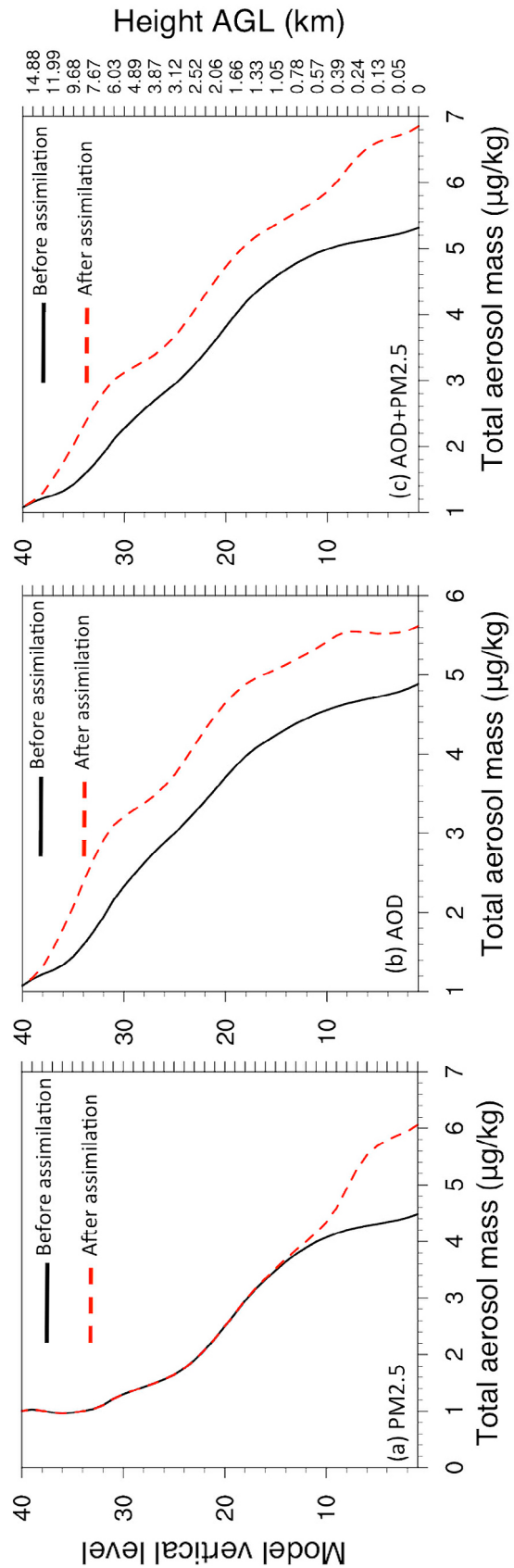


Figure 3. Total aerosol mass mixing ratio ($\mu\text{g}/\text{kg}$) for each vertical level before (solid lines) and after (dashed lines) DA averaged over all locations where PM_{2.5} DA occurred, for the (a) PM_{2.5}, (b) AOD, and (c) AOD+PM_{2.5} experiments, averaged over all 1800 UTC analyses. Values on the right side of Figure 3c indicate the approximate height (AGL) of each model level (km).

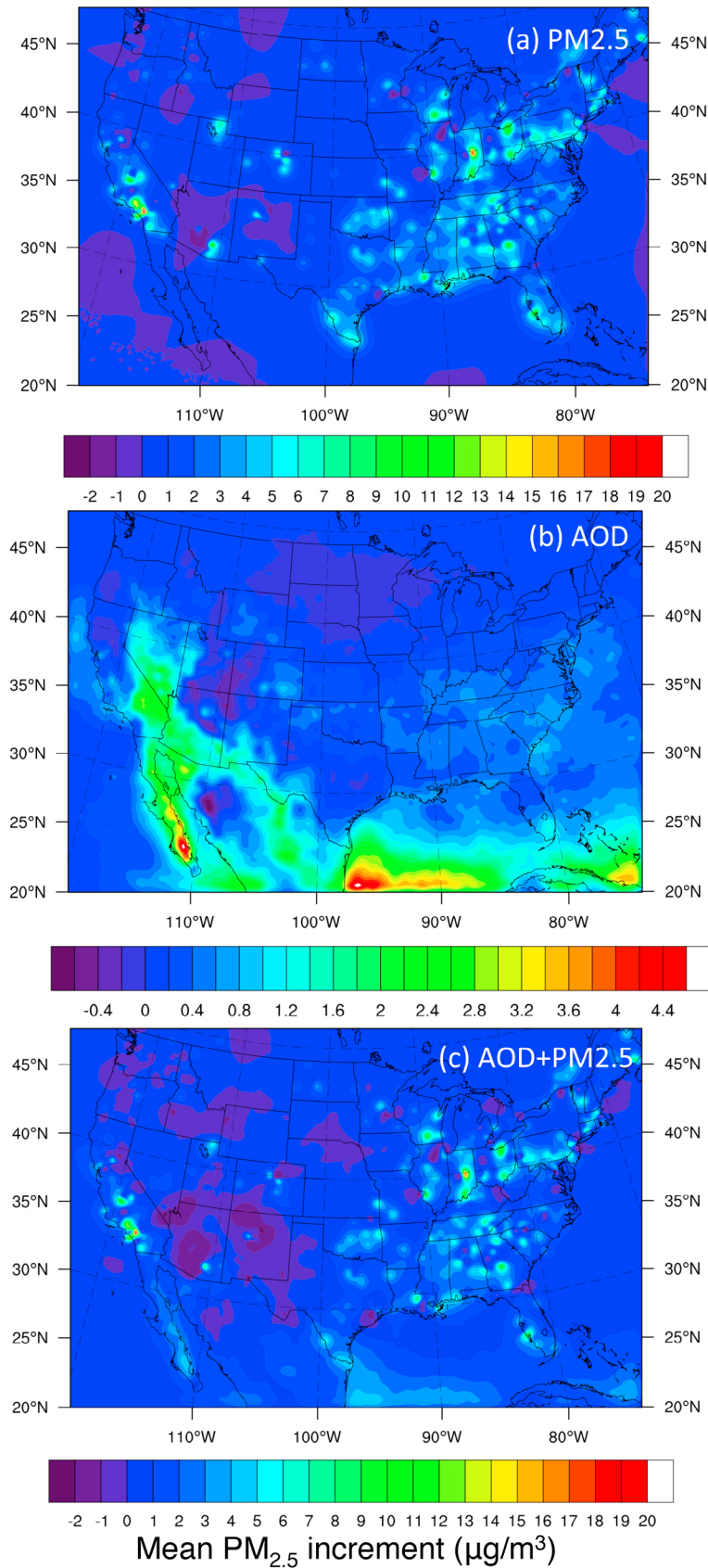


Figure 4. Average 1800 UTC PM_{2.5} analysis increments at the lowest model level for the (a) PM_{2.5}, (b) AOD, and (c) AOD+PM_{2.5} experiments. Note that the color scale in Figure 4b differs from that of the other panels to more easily highlight differences.

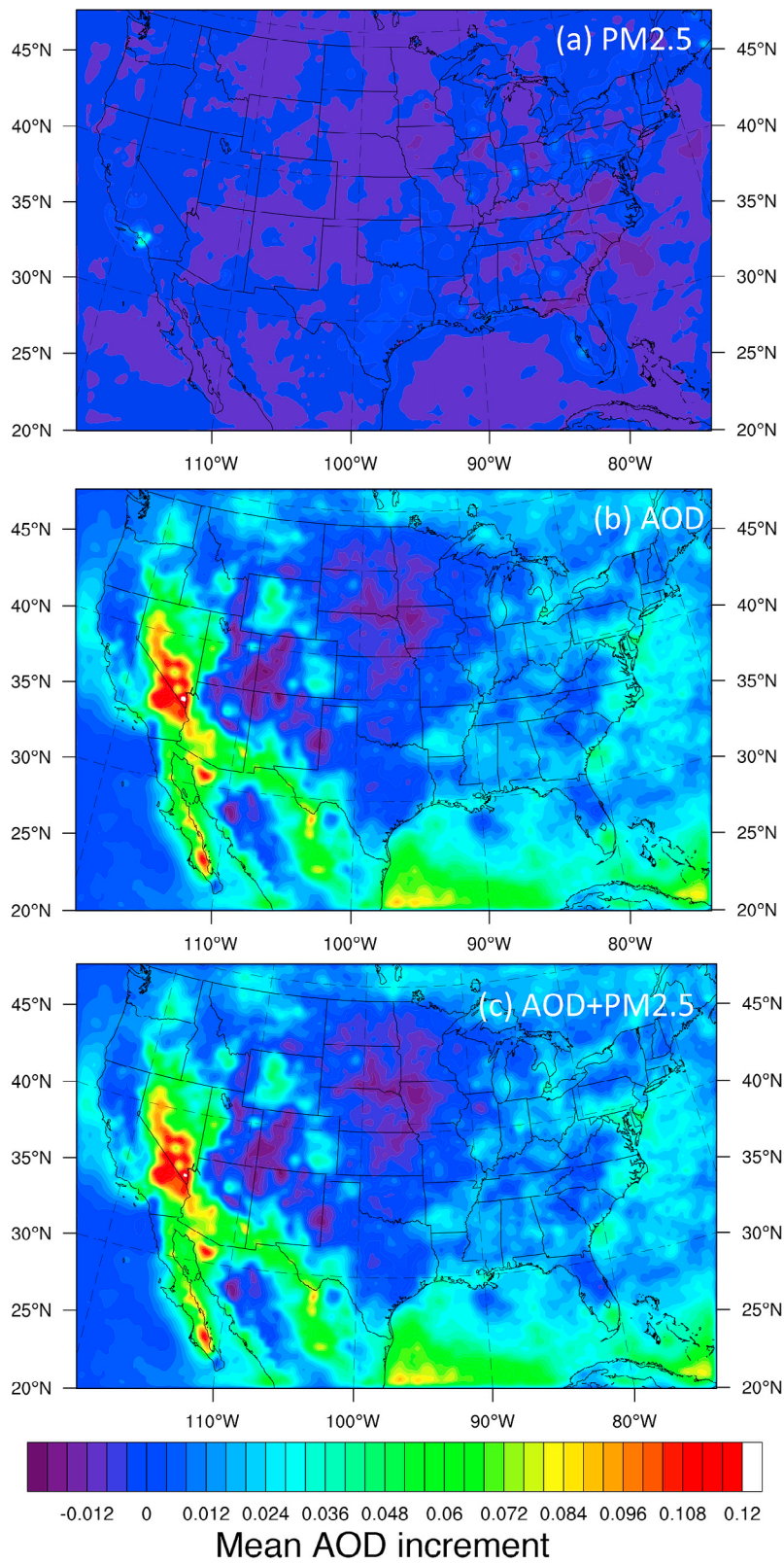


Figure 5. As in Figure 4, except the increments are for total column-integrated AOD at 550 nm.

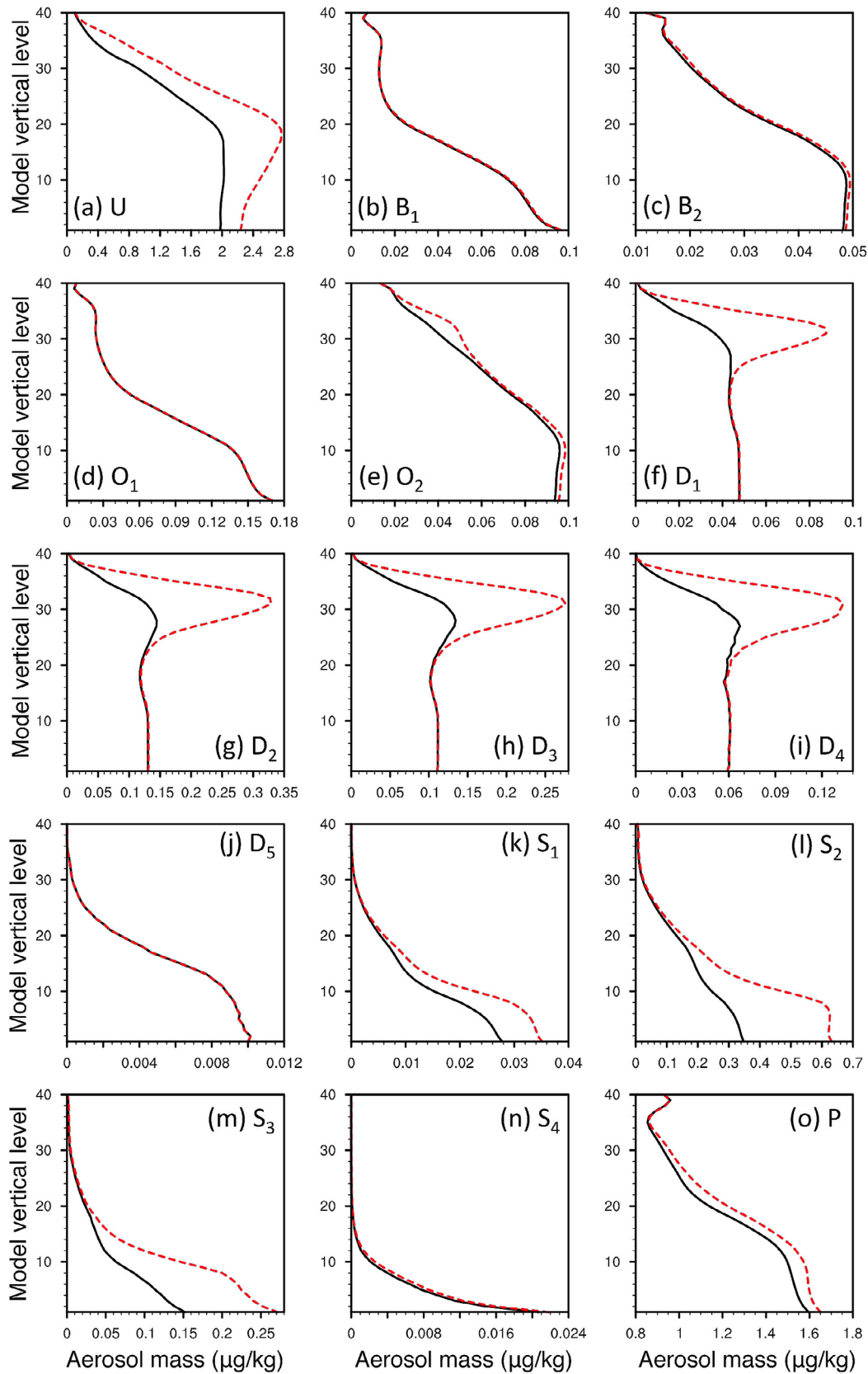


Figure 6. As in Figure 3, except for the experiment that only assimilated AOD and for (a) sulfate, (b) hydrophobic BC, (c) hydrophilic BC, (d) hydrophobic OC, (e) hydrophilic OC, (f–j) dust aerosols in increasing size bins, (k–n) sea salt aerosols in increasing size bins, and (o) unspecified contributions to PM_{2.5}.

Table 1. Standard 2 × 2 Contingency Table for Dichotomous Events

Forecast	Observed		Marginal Total
	Yes	No	
Yes	<i>a</i>	<i>b</i>	<i>a + b</i>
No	<i>c</i>	<i>d</i>	<i>c + d</i>
Marginal Total	<i>a + c</i>	<i>b + d</i>	

forecast every 6 h between 0000 UTC 01 June and 1800 UTC 14 July (inclusive). The forecasts were integrated for 6 h, except the 1800 UTC initializations—when AOD DA had its greatest impact—which produced 48-h forecasts.

[36] The three experiments that assimilated observations performed a new aerosol analysis every 6 h to update the control variables before initializing WRF-Chem forecasts. The first analyses used the 0000 UTC 01 June fields as backgrounds, while subsequent analyses used the previous cycle's 6-h aerosol forecasts as backgrounds. The experiment without DA initialized its first forecast from the 0000 UTC 01 June fields, while initial aerosol fields for future forecasts were simply taken from the previous cycle's 6-h forecast.

[37] Every 6 h, the initial meteorological fields of all four experiments were updated by interpolating 20-km NAM analyses onto the computational domain. No meteorological DA was performed. Thus, the initial meteorology was the same for each experiment, and the experiments only differed regarding the type of aerosol observations (if any) that were assimilated, permitting a clear isolation of the impact of aerosol DA on WRF-Chem forecasts.

[38] The analyses and forecasts from the four experiments were compared to AOD observations from MODIS and AERONET, as well as surface PM_{2.5} measurements from AIRNow. The results of these comparisons are now described.

6. Results

[39] WRF-Chem analyses and forecasts of PM_{2.5} and AOD are now analyzed. The DA impact is examined before verifying forecasts. Although forecasts were produced every 6 h, we focus on evaluating the 1800 UTC analyses and subsequent 48-h forecasts.

6.1. Impact on Analyses

[40] The total aerosol mass mixing ratio (sum of the 15 control variables) was averaged over all grid points where PM_{2.5} DA occurred and temporally averaged over all 1800 UTC analyses (44 total) at each vertical level to assess the impact of DA. When PM_{2.5} or AOD was assimilated, the mean total aerosol mass increased after DA (Figure 3). However, the mass increase was confined below model level 14 (~1.0 km AGL) when only surface PM_{2.5} observations were assimilated (Figure 3a), and the mass increase diminished rapidly above the 6th model level (~0.24 km AGL). Conversely, assimilating AOD with and without PM_{2.5} increased the total aerosol mass throughout the column (Figures 3b and 3c). Directly assimilating PM_{2.5} increased the surface aerosol mass the most (~1.5 μg/kg). Solely assimilating AOD also increased the surface aerosol mass,

but the increase was smaller (~0.7 μg/kg) since the increment was spread over a deeper layer.

[41] The spatial distribution of the average 1800 UTC PM_{2.5} analysis increments at the lowest model level (Figure 4) further reveals very different impacts of AOD and PM_{2.5} DA. When only surface PM_{2.5} observations were assimilated (Figure 4a) the mean increments were mostly positive, indicating PM_{2.5} DA primarily increased the model PM_{2.5}, consistent with Figure 3a. Assimilating just PM_{2.5} produced mainly localized increment structures around the AIRNow sites, and the PM_{2.5} gradients near the sites on individual days were much sharper than the means shown in Figure 4.

[42] On the other hand, solely assimilating AOD produced smaller surface PM_{2.5} increments (Figure 4b) over most of the domain (note the different color scale compared to Figures 4a and 4c). The largest surface PM_{2.5} increments occurred over the Gulf of Mexico, Mexico, and southwest CONUS, and the increments were broader and smoother compared to those generated by assimilating just PM_{2.5}, reflecting the expansive coverage of the satellites. Simultaneously assimilating AOD and PM_{2.5} (Figure 4c) generated surface PM_{2.5} increments that mostly resembled the increments when just PM_{2.5} was assimilated, but influence of AOD DA was also evident.

[43] The mean 1800 UTC column-integrated 550 nm total AOD increments were also computed (Figure 5). As PM_{2.5} DA only modified a small portion of the column (Figure 3a), the average total AOD increments were near zero (Figure 5a) over most of the domain when just PM_{2.5} observations were assimilated. But, when AOD was assimilated, either alone or with PM_{2.5} observations (Figures 5b and 5c), the AOD field was modified more substantially. The largest increments were produced over the Gulf of Mexico, Atlantic Ocean, Mexico, and relatively low elevations of the southwest CONUS.

[44] It is also interesting to examine how DA impacted the individual aerosol species. Figure 6 is similar to Figure 3, except it shows the mixing ratios of each control variable before and after DA for the experiment that only assimilated AOD. AOD DA increased sulfate (Figure 6a) and unspiciated contributions to PM_{2.5} (Figure 6o) throughout the column, while concentrations of BC (Figures 6b and 6c), hydrophobic OC (Figure 6d), and dust and sea salt in the largest size bins (Figures 6j and 6n) were unchanged. Sea salt mixing ratios in the three smallest size bins (Figures 6k–6m) increased substantially below the 20th model level. Hydrophilic OC concentrations increased slightly after DA (Figure 6e) and mixing ratios of dust aerosols in the four smallest size bins (Figures 6f–6i) increased near the tropopause. Since MODIS AOD observations provide no information regarding speciation, these different behaviors were primarily driven by the background and observation error covariances.

[45] When only PM_{2.5} was assimilated, consistent with Figure 3a, mass concentrations of all control variables were unchanged above the 14th model level (not shown). Additionally, mixing ratios of coarse dust and sea salt species (bins with effective diameters >2.5 μm) were constant before and after DA since they did not contribute to PM_{2.5} and the BECs were univariate. Otherwise, below the 14th model level, the impact of solely assimilating PM_{2.5} was

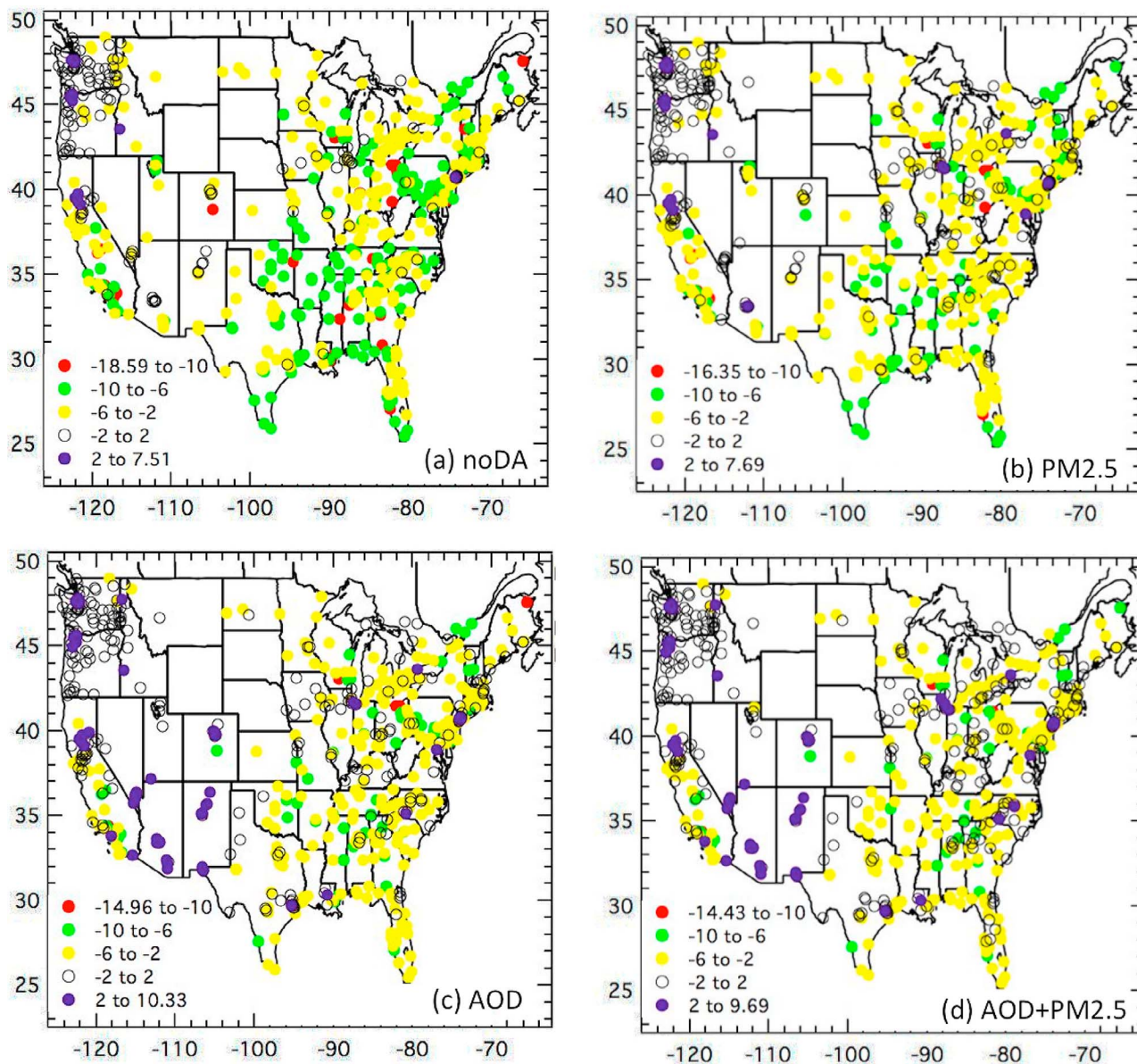


Figure 7. Average bias at selected AIRNow sites computed from averaging hourly 0–24-h forecasts and comparing them to the corresponding 24-h average observations, aggregated over the experimental period for the (a) noDA, (b) PM_{2.5}, (c) AOD, and (d) AOD+PM_{2.5} experiments.

qualitatively similar to that of just assimilating AOD, with mixing ratios of sulfate, sea salt in the two smallest size bins (effective diameters <2.5 μm), and unspiciated contributions to PM_{2.5} increasing the most (not shown).

[46] AOD DA impacted the aerosol fields throughout the column while the impact of PM_{2.5} DA was confined to lower model levels. Both PM_{2.5} and AOD DA increased the surface aerosol mass fields, but the impacts were more pronounced with PM_{2.5} DA. The surface PM_{2.5} increments that were generated when AOD and surface PM_{2.5} were assimilated concurrently reflected the combined impacts of individual AOD and PM_{2.5} DA. The changes to aerosol ICs due to DA manifested themselves in the forecasts, which are now discussed.

6.2. Aerosol Forecast Verification

[47] The WRF-Chem forecasts were verified using a variety of metrics. Let O_m and F_m denote the respective observed and forecast values of either PM_{2.5} or AOD at the m th of N locations. Many statistics assessing forecast accuracy can be defined based on the correspondence between the model and observations. The additive bias (B) is simply the difference of the mean and observed values, expressed as

$$B = \frac{1}{N} \sum_{m=1}^N (F_m - O_m) = \bar{F} - \bar{O}, \quad (8)$$

where the overbars denote averages. B can be considered a measure of systematic model error but does not quantify how individual forecast-observation pairs agree. However, the

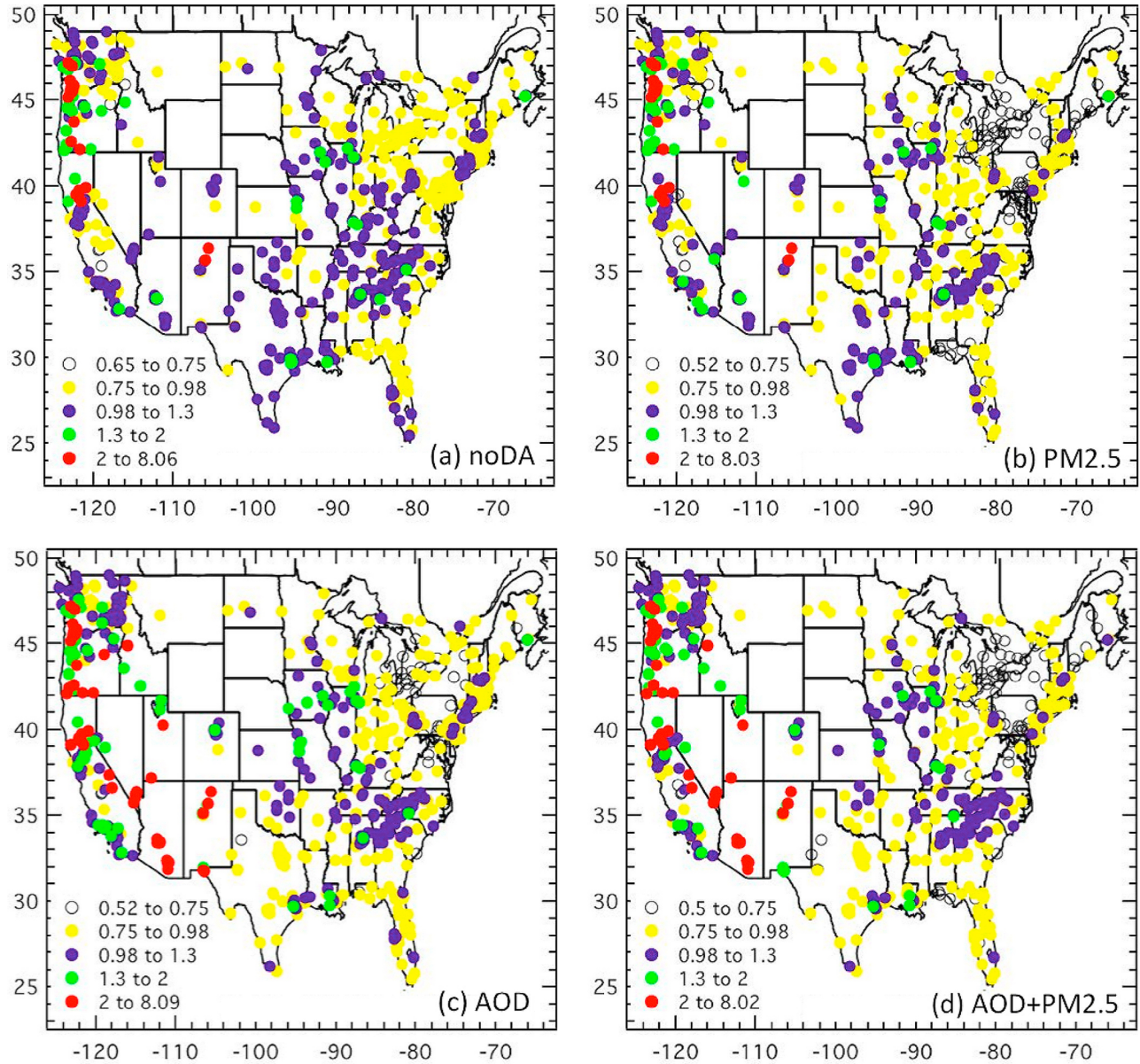


Figure 8. As in Figure 7 except de-biased RMSE normalized by each site's mean standard deviation of the observations.

de-biased root mean square error ($RMSE_{de-biased}$) quantifies this correspondence, which is defined as

$$RMSE_{de-biased} = \sqrt{\frac{1}{N} \sum_{m=1}^N (F_m - O_m - B)^2}, \quad (9)$$

and can be interpreted as a measure of non-systematic model error. Additionally, the linear correspondence between the forecast and observations is quantified by the correlation coefficient (r):

$$r = \frac{\sum_{m=1}^N (F_m - \bar{F})(O_m - \bar{O})}{\sqrt{\sum_{m=1}^N (F_m - \bar{F})^2} \sqrt{\sum_{m=1}^N (O_m - \bar{O})^2}}. \quad (10)$$

[48] To evaluate the experiments' ability to discriminate between events, with the assistance of a 2×2 contingency table (Table 1), the equitable threat score (ETS) was calculated for model forecasts of PM_{2.5} at the AIRNow sites. By selecting PM_{2.5} thresholds for the forecasts (q_f) and observations (q_o) to define an event, the m th site was placed into the proper quadrant of Table 1 based on the correspondence between the forecast and observations at its location. Specifically, the m th site fell into category a if the event was correctly predicted ($F_m \geq q_f$ and $O_m \geq q_o$); b if the event was forecast but did not occur ($F_m \geq q_f$ and $O_m < q_o$); c if an event occurred but was not forecast ($F_m < q_f$ and $O_m \geq q_o$); and d if a nonevent was correctly predicted ($F_m < q_f$ and $O_m < q_o$). Using the elements of Table 1, ETS is defined as $ETS = (a - e)/(a + b + c - e)$, where $e = (a + b)(a + c)/(a + b + c + d)$ and is the number of "hits" (elements in

quadrant “a” of Table 1) due to random chance. ETS ranges from $-1/3$ to 1, with a perfect forecast achieving a score of 1 and a forecast worse than random chance scoring less than 0. In many applications, $q_f = q_o$, but equality of the two thresholds is not required.

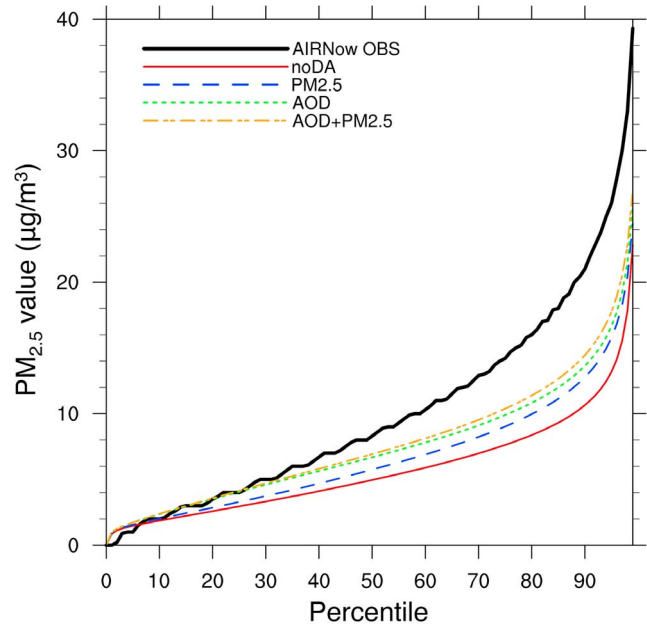
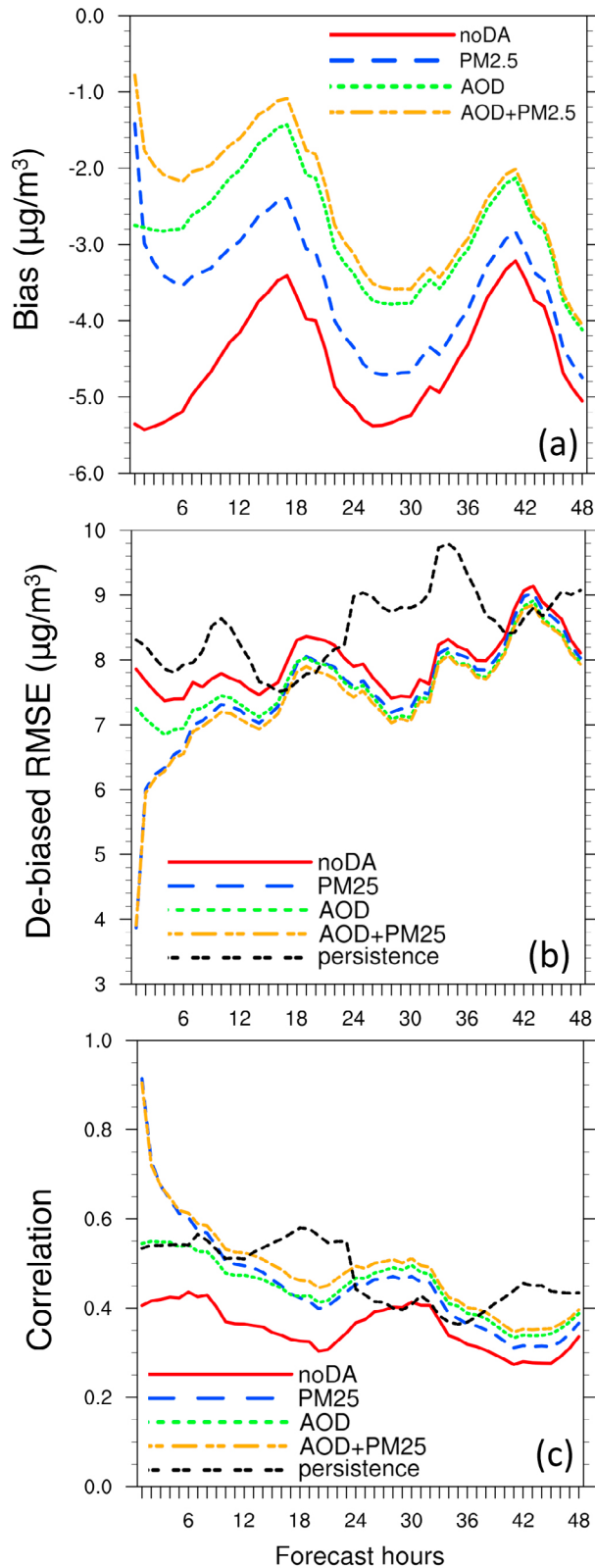


Figure 10. PM_{2.5} climatology: PM_{2.5} percentiles (0–99%) calculated separately for the observations and each experiment over the entire experimental period (see text).

6.2.1. Verification of Surface PM_{2.5} Forecasts

[49] Model forecasts of PM_{2.5} were verified against AIRNow observations across the domain (Figure 1). Model output at the lowest vertical level was assumed to correspond with the surface AIRNow measurements, and the model PM_{2.5} fields were interpolated to the locations of the AIRNow sites for verification.

[50] There were important geographic differences regarding forecast performance. Figure 7 shows the mean bias at selected sites computed from averaging hourly 0–24-h surface PM_{2.5} forecasts and comparing them to the corresponding 24-h average AIRNow values and aggregating over all 1800 UTC forecasts. The control experiment (Figure 7a) had primarily negative biases, indicating WRF-Chem under-predicted surface PM_{2.5}. At many locations in the eastern half of the domain, all forms of DA (Figures 7b–7d) improved the biases (though they were still mainly negative), while DA led to little improvement in the northwest CONUS. Over the

Figure 9. (a) Bias ($\mu\text{g}/\text{m}^3$), (b) de-biased RMSE ($\mu\text{g}/\text{m}^3$), and (c) correlation coefficient of surface PM_{2.5} forecasts as a function of forecast hour, summed over all AIRNow locations (except those within the excluded region in Figure 1) and aggregated over all 1800 UTC forecasts. Model values are hourly averages between consecutive top-of-the-hours. Labels on the x-axis refer to ending times of the averaging periods (e.g., “12” means the average of the model PM_{2.5} forecast between the 11th and 12th forecast hours). Persistence was computed by “forecasting” yesterday’s hourly PM_{2.5} observations twice over the 48-h forecast period (i.e., the persistence forecasts for the 12th and 36th forecast hours were identical). The bias for domain-averaged persistence is close to zero, and therefore, persistence was not plotted in Figure 9a.

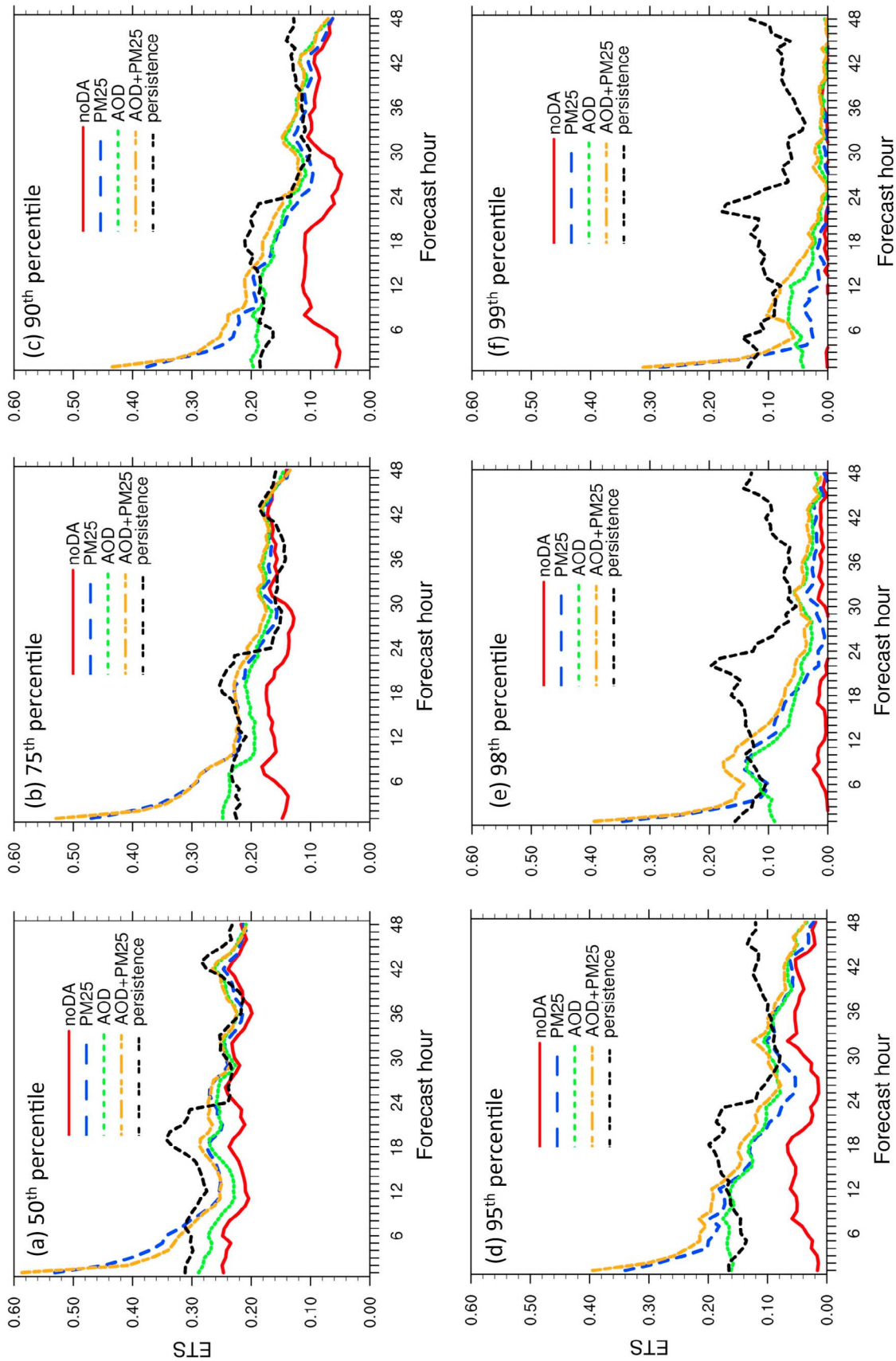


Figure 11. As in Figure 9, except ETSs computed using climatological thresholds of (a) 50%, (b) 75%, (c) 90%, (d) 95%, (e) 98%, and (f) 99%.

Table 2. Aggregate Verification Statistics for 24-h AOD Forecasts Compared to MODIS AOD Values

Experiment	Bias	De-biased RMSE	Correlation Coefficient
noDA	-0.114	0.125	0.288
PM2.5	-0.109	0.124	0.306
AOD	-0.044	0.134	0.318
AOD + PM2.5	-0.044	0.134	0.319

southwest CONUS, AOD DA, either alone or with PM_{2.5} DA (Figures 7c and 7d), produced extremely high biases at many sites, while assimilating just PM_{2.5} yielded few differences at these locations compared to when no observations were assimilated.

[51] Figure 8 shows the corresponding de-biased RMSEs normalized by each site's mean standard deviation of the observations (to more easily reveal differences). The patterns were similar to those of the biases (Figure 7) and correlation coefficients (not shown). Aerosol DA (Figures 8b–8d) realized improvements at many sites east of 104°W compared to when no assimilation occurred (Figure 8a). Only assimilating AOD improved the forecasts in eastern Texas more than just assimilating PM_{2.5}, while solely assimilating PM_{2.5} led to better forecasts than only assimilating AOD in the northeast CONUS and southern Canada. Assimilating AOD and PM_{2.5} simultaneously yielded forecasts that reflected the best aspects of both individual PM_{2.5} and AOD DA over these two areas. In the southwest CONUS, assimilating just PM_{2.5} did not improve the bias-removed RMSEs compared to the control, and AOD DA, with and without concurrent PM_{2.5} DA, degraded the forecasts. The forecast degradation in the southwest CONUS due to AOD DA is discussed in section 7.

[52] Hourly PM_{2.5} forecasts were also verified to evaluate the temporal evolution of forecast accuracy. Additionally, verification scores were computed for previous-day persistence by “forecasting” yesterday's hourly PM_{2.5} observations twice over the 48-h forecast period (for example, the persistence forecasts for the 12th and 36th forecast hours were identical). As the AIRNow values represent hourly averages with effective valid times of 30 min past each hour, hourly WRF-Chem PM_{2.5} forecasts valid at consecutive top-of-the-hours were averaged for comparison with observations. In Figures 9 and 11, values on the *x*-axis denote ending periods of the 1-h averages (e.g., a value of 6 means the average between the 5- and 6-h forecasts). Given the poor forecast performance due to AOD DA over the southwest CONUS (Figures 7 and 8), all subsequent verification did not consider forecasts within 104–116°W and 30–40°N (hereafter the “excluded region”; see the box in Figure 1) to prevent bad forecasts at a small number of sites from dominating statistics.

[53] The bias, de-biased RMSE, and correlation coefficient were calculated for PM_{2.5} forecasts aggregated over all 1800 UTC forecasts and AIRNow sites (outside the excluded region). All experiments had a negative bias for all times (Figure 9a). The differences between the experiments decreased for longer forecasts, likely due to model processes and emissions dominating at later periods [Kahnert, 2008]. The negative bias was largest without DA, but when observations were assimilated the negative bias was reduced for all forecast hours. After the first hour, assimilating only AOD

reduced the bias more than just assimilating PM_{2.5}. Up to ~42 h, the experiment with both PM_{2.5} and AOD assimilation produced the smallest bias, illustrating the benefit of assimilating observations from multiple sources.

[54] While the bias measures systematic error, the de-biased RMSE (Figure 9b) assesses non-systematic model error. Aerosol DA improved the bias-removed RMSEs compared to the control for all times, although the differences between the experiments were very small after ~36 h. In the first ~15 h, assimilating just PM_{2.5} generated lower de-biased RMSEs than assimilating only AOD, but after ~24 h, assimilating solely AOD produced similar or slightly better scores than assimilating just PM_{2.5}. Assimilating both PM_{2.5} and AOD yielded the lowest de-biased RMSEs through ~30 h. Additionally, when PM_{2.5} was assimilated, rapid error growth occurred in the first hour (see section 7 for a discussion). All experiments produced lower de-biased RMSEs than persistence for most forecast hours.

[55] The correlation coefficients (Figure 9c) generally corresponded to the de-biased RMSEs. In the first 6 h, PM_{2.5} DA, with or without AOD DA, produced the highest correlations. Thereafter, correlations were best when both AOD and PM_{2.5} were assimilated. For the first ~15 h, assimilating only PM_{2.5} increased correlations more than assimilating just AOD; after ~15 h the opposite held. Similar to the biased-removed RMSEs, correlations of the four experiments grew closer with time. Persistence always produced higher correlations than the control, but the experiment that assimilated both PM_{2.5} and AOD had higher correlations than persistence for the first ~12 h and between ~24–36 h.

[56] Clearly, the GOCART option within WRF-Chem systematically underpredicted the surface aerosol mass, which was also noted by LIU11. The PM_{2.5} climatology over the experimental period (0000 UTC 01 June to 1800 UTC 14 July) further illuminates the model biases. All AIRNow observations outside of the excluded region (Figure 1) over the experimental period were included in the observational climatology. Similarly, model PM_{2.5} values predicted at the non-excluded AIRNow locations each forecast hour from all 1800 UTC initializations were included in the model climatologies. The *z*th percentile (e.g., 95th percentile) was chosen to determine the climatological absolute PM_{2.5} values corresponding to the *z*th percentile (*q_z*) separately for the observations and each experiment. For example, considering the AIRNow climatology, *z* percent of all PM_{2.5} AIRNow observations were <*q_z*.

[57] All forms of aerosol DA increased the absolute PM_{2.5} concentrations compared to the control. At percentiles >5% (Figure 10), the experiments without or with just PM_{2.5} DA had the lowest absolute PM_{2.5} values compared to the observations. The two experiments that assimilated AOD produced the highest model PM_{2.5} values, with climatologies similar to the observations for the 5th–30th percentiles. Simultaneous PM_{2.5} and AOD DA produced percentiles closest to those observed, but for percentiles >30%, the observed absolute concentrations were still substantially higher than those of any experiment. Overall, the percentiles reveal the underprediction of PM_{2.5} concentrations for all experiments, particularly for more extreme events, and are consistent with the biases (Figure 9a).

[58] These percentiles were also used in the computation of the ETS (Figure 11). Using percentile thresholds rather than

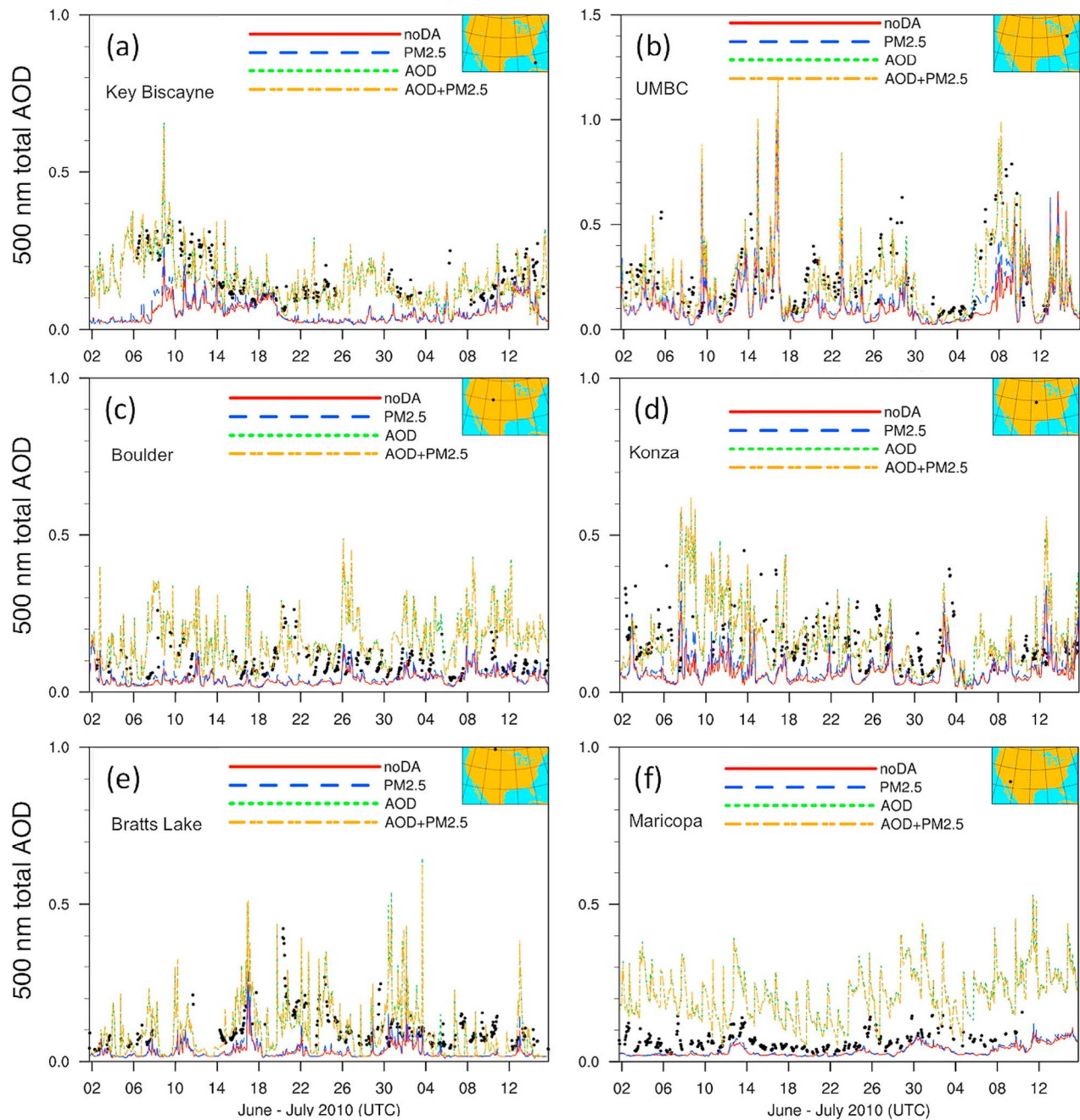


Figure 12. Hourly time series of total AOD at 500 nm from 0000 UTC 01 June to 1700 UTC 15 July at the (a) Key Biscayne, (b) UMBC, (c) Boulder, (d) Konza, (e) Bratts Lake, and (f) Maricopa AERONET sites. Model values represent output every hour beginning at the initial time and ending at the 23rd hour of integration patched together for each 1800 UTC forecast. AERONET observations represent hourly averages.

absolute thresholds removes the impact of bias when calculating skill scores and permits a clear assessment of spatial skill [e.g., *Lean et al.*, 2008; *Roberts and Lean*, 2008; *Schwartz et al.*, 2009; *Mittermaier and Roberts*, 2010]. For example, to compute the ETS for the 90th percentile, $q_o = 21.0 \mu\text{g}/\text{m}^3$, while q_f varied depending on the experiment between 10.65 and 14.45 $\mu\text{g}/\text{m}^3$ (see Figure 10). The ETSs were calculated considering all AIRNow sites except those in the excluded region and aggregated over all 1800 UTC forecasts.

[59] As the event became rarer and the forecast length increased, ETSs decreased (Figure 11). At the 50th and 75th percentiles (Figures 11a and 11b), all forms of DA improved forecasts compared to the control through ~ 30 h. Just assimilating PM_{2.5} produced better forecasts than only assimilating AOD through ~ 18 h, with comparable scores between the two experiments thereafter. At these percentiles, when both AOD and PM_{2.5} were assimilated, ETSs were nearly identical to those when just PM_{2.5} was assimilated and

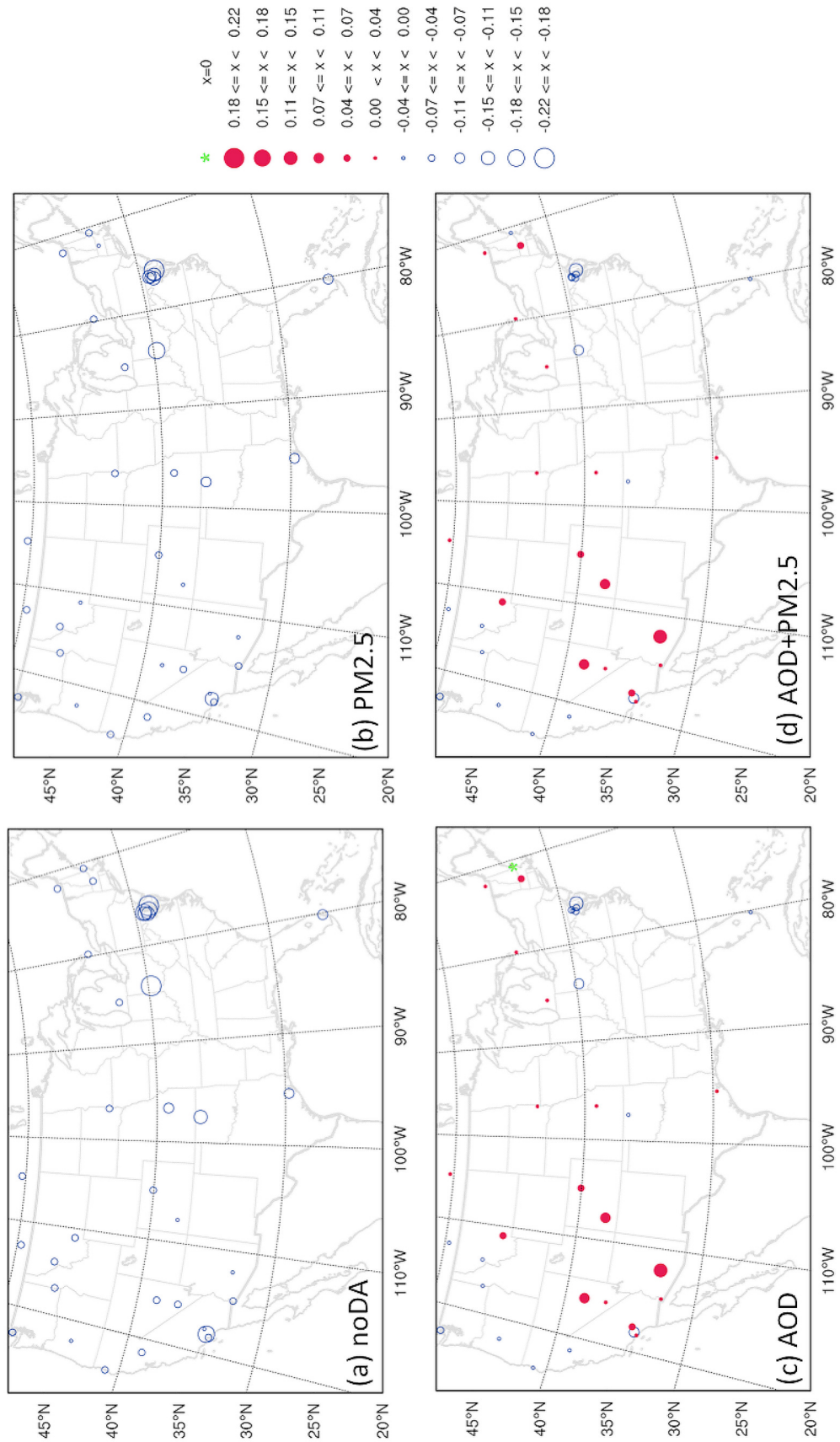


Figure 13. Mean biases computed from hourly 0–23-h forecasts from all 1800 UTC initializations and the corresponding hourly averaged AERONET observations at all 34 AERONET sites for the (a) noDA, (b) PM_{2.5}, (c) AOD, and (d) AOD + PM_{2.5} experiments. In the legend, “x” refers to the bias.

comparable or higher than persistence ETSS for most times. For the 90th, 95th, and 98th percentiles (Figures 11c–11e), aerosol DA led to better forecasts than the control for at least ~36 h, with the combination of AOD and PM_{2.5} DA yielding the highest ETSS for ~24 h. Only assimilating PM_{2.5} produced higher ETSS than solely assimilating AOD for ~12–18 h. After this time, just assimilating AOD yielded similar or slightly higher scores than only assimilating PM_{2.5}. Assimilating both AOD and PM_{2.5} produced better ETSS than persistence for the first ~12 h. For the most extreme events (Figure 11f), assimilating only AOD generated better forecasts than just PM_{2.5} DA for ~6–18-h forecasts. However, the best forecasts through ~18 h occurred when AOD and PM_{2.5} were assimilated concurrently. No experiment had skill compared to random forecasts past ~24 h at the 99th percentile.

[60] Generally, simultaneously assimilating PM_{2.5} and AOD produced ETSS that were either the highest or tied for highest, but there was little skill for extreme events. When ETSS were computed using identical thresholds for the observations and forecasts (i.e., $q_f = q_o$), the results did not qualitatively differ, although ETSS were lower than those in Figure 11 for all but the lowest PM_{2.5} thresholds (not shown).

[61] The forecasts of AOD are now evaluated.

6.2.2. Verification of AOD Forecasts

[62] Forecasts of AOD were verified against MODIS AOD observations and at AERONET sites. Statistics comparing 24-h forecasts of model AOD with MODIS AOD aggregated over all 1800 UTC forecasts outside the excluded region are shown in Table 2. Assimilating AOD reduced the negative AOD bias, although AOD DA slightly worsened the de-biased RMSE. However, AOD DA led to the highest correlations, even though the values were low. Just assimilating PM_{2.5} observations produced little change compared to the control. These metrics indicate that 24-h forecasts of AOD have room for improvement, but AOD DA reduced the bias and increased the correlation with observations.

[63] The AOD forecasts were also verified against AERONET observations. During the experimental period, data from 34 AERONET sites were available over the domain (Figure 1). Figure 12 shows model predictions of total 500 nm AOD at several sites and the corresponding AERONET observations. Model values represent output every hour beginning at the initial time and ending at the 23rd hour of integration patched together for each 1800 UTC forecast, and the AERONET values are hourly averaged. PM_{2.5} DA had little impact on AOD forecasts compared to the control. But, at all sites, AOD values were increased by assimilating AOD, and the higher values generally agreed better with observations (Figures 12a, 12b, 12d, and 12e). However, at the Boulder, Colorado site (Figure 12c), AOD DA sometimes led to overpredictions, such as after 4 July. Moreover, at Maricopa, Arizona (Figure 12f), AOD DA produced forecasts that consistently and severely over-predicted AOD.

[64] This overprediction from AOD DA was also observed at other AERONET sites in the southwest CONUS, consistent with the high surface PM_{2.5} biases and poor forecasts over this region. The average biases computed from all 1800 UTC 0–23-h model forecasts and AERONET observations over the experimental period are shown in Figure 13. AOD DA led to high biases in the southwest CONUS that were

much worse than the biases of the control (Figures 13c and 13d). However, AOD DA reduced the mean bias at most sites outside this region compared to the control (Figure 13a). PM_{2.5} DA (Figure 13b) resulted in little difference compared to when no DA occurred.

[65] AOD forecasts were mostly improved by AOD DA, except over the southwest CONUS. The cause of the high bias over the southwest CONUS due to AOD DA and a general discussion of the results are presented in the next section.

7. Discussion

[66] Despite mostly encouraging results from both AOD and PM_{2.5} DA, several disconcerting features were noted. For example, there was clearly a low WRF-Chem bias of aerosol mass. Missing secondary organic aerosol (SOA) formation, nitrate, and ammonium within the GOCART aerosol model likely contributed to the low model bias. OC is known to contribute at least 50% to PM_{2.5}, and SOA is a dominant component of OC [Zhang *et al.*, 2007]. Global model [Volkamer *et al.*, 2006] and regional U.S. multimodel studies [e.g., McKeen *et al.*, 2009] have documented the consistent underprediction of OC in models that do not include SOA formation. These results suggest that both AOD and PM_{2.5} DA can partially remedy inherent model biases.

[67] It is also noteworthy that rapid error growth occurred in the first hour whenever surface PM_{2.5} observations were assimilated but not when just AOD was assimilated (Figures 9b, 9c, and 11). Furthermore, it is intriguing that only assimilating AOD produced smaller surface PM_{2.5} biases (Figure 9a) after the first hour and comparable or slightly better surface PM_{2.5} forecasts after ~15–18 h compared to when just PM_{2.5} was assimilated. All these behaviors can be attributed to model processes and the structures of the analysis fields.

[68] As evidenced by the mean surface PM_{2.5} increments, whenever PM_{2.5} was assimilated sharp horizontal aerosol mass gradients were generated in the analyses near the AIRNow sites (Figures 4a and 4c). But, when only AOD was assimilated, the horizontal gradients were much weaker (Figure 4b). Similarly, as AOD DA increased aerosol mass throughout the column, vertical aerosol mass gradients below ~1-km were weakest in the analyses when just AOD was assimilated (Figure 3b). Although simultaneous DA of AOD and PM_{2.5} also increased aerosol mass throughout the column, contributions from the PM_{2.5} observations increased aerosol mass the most near the surface (Figure 3c) and the vertical aerosol mass gradient was larger below ~1-km compared to when only AOD was assimilated. However, the vertical aerosol mass gradient was strongest below ~1-km in the analyses when just PM_{2.5} was assimilated (Figure 3a).

[69] Once model integration began, advection, diffusion, and vertical mixing smoothed the aerosol mass gradients. Sharper gradients enhance these processes. Thus, whenever PM_{2.5} observations were assimilated, horizontal advection and diffusion quickly smoothed the strong horizontal gradients and diluted surface aerosol mass near the AIRNow sites, leading to the rapid error growth in the first hour. Vertical mixing also contributed to the error growth in the first hour whenever PM_{2.5} observations were assimilated by transporting lower aerosol concentrations above the surface

downward. Conversely, as solely assimilating AOD yielded smaller near-surface horizontal and vertical aerosol mass gradients, vertical mixing and horizontal advection and diffusion were weaker, leading to quite stable surface PM_{2.5} values over the first hour. Furthermore, only assimilating AOD produced higher above-surface aerosol mixing ratios than just PM_{2.5} DA. Therefore, vertical mixing transported higher aerosol values to the surface when solely AOD was assimilated compared to when only PM_{2.5} DA occurred, leading to a smaller surface PM_{2.5} bias after the first hour in the experiment that just assimilated AOD than the experiment only assimilating PM_{2.5}. It is likely the experiment that performed just AOD DA produced similar or slightly better surface PM_{2.5} forecasts after ~15–18 h than the experiment that only assimilated PM_{2.5} due to its improved surface bias.

[70] Assimilation parameters can be tuned to lessen the effects of these model processes when surface PM_{2.5} is assimilated and reduce the rapid error growth in the first hour. For instance, vertical BEC length scales could be increased to permit deeper increments from PM_{2.5} DA and diminish the impact of vertical mixing. Similarly, increasing the horizontal BEC length scales would allow assimilation of PM_{2.5} observations to influence a broader area, decreasing the magnitudes of horizontal advection and diffusion during model integration. However, it is unclear whether increasing these length scales is physically justifiable. Additionally, the PM_{2.5} observation error could be increased to weight the analysis closer to the background.

[71] Last, AOD DA degraded PM_{2.5} and AOD forecasts in the southwest CONUS, where the AOD increments were largest (Figures 5b and 5c). These large increments indicate the analyses fit very closely to the MODIS AOD values over these areas. The large increments closely followed the topographic contours (Figure 1) and were mostly generated over relatively low, flat areas in arid, desert-like regions. Summertime in these locales features high surface reflectance, which can interfere with MODIS AOD cloud masking algorithms and adversely impact retrieval values [Engel-Cox *et al.*, 2004; Zhang and Reid, 2006; Drury *et al.*, 2008]. In fact, due to high surface reflectance, Engel-Cox *et al.* [2004] found that MODIS AOD and surface PM_{2.5} values were only weakly correlated in the western CONUS, despite good correspondence in the eastern half of the CONUS. Similarly, Prados *et al.* [2007] found poor correlations between AERONET and MODIS AOD over the western CONUS. Moreover, they found low correlations over the desert southwest between MODIS AOD and AOD calculated from the Geostationary Operational Environmental Satellite-12 (GOES-12) Aerosol Smoke Product (GASP), which reduces confidence in MODIS AOD values over that region. Additionally, Drury *et al.* [2008, 2010] found that MODIS AOD retrievals are biased high over arid regions since the MODIS algorithm underestimates surface reflectance and introduced a method to better quantify surface reflectance and improve MODIS AOD retrievals. Furthermore, Zhang *et al.* [2005] and Zhang and Reid [2006] noted that MODIS AOD was biased high over bright areas. To remedy this bias (and other biases), they developed empirical corrections and quality assurance procedures to correct raw MODIS AOD values.

[72] Given these findings, it appears that issues regarding MODIS AOD data quality over the southwest CONUS led to poor analyses in these regions and subsequently erroneous

forecasts, underscoring the need for careful QC of MODIS AOD. Clearly, additional development following Zhang and Reid [2006] and Drury *et al.* [2008, 2010] is needed within GSI to either better use or reject MODIS AOD retrievals over arid regions.

8. Summary

[73] MODIS total AOD retrievals and surface PM_{2.5} observations from the AIRNow network were assimilated every 6 h using 3DVAR between 01 June and 14 July 2010. Each 1800 UTC analysis initialized a 48-h WRF-Chem forecast over a domain spanning the CONUS. Parallel experiments assimilated AOD and PM_{2.5} both separately and together and a control experiment that did not employ DA was also performed.

[74] The 1800 UTC forecasts were validated against MODIS, AERONET, and AIRNow observations. All experiments had a low surface bias of aerosol mass mixing ratio that was primarily caused by the WRF-Chem model. However, assimilating both AOD and PM_{2.5} observations separately and together helped reduce the low bias. Just assimilating AOD improved the surface bias more than only assimilating PM_{2.5} after the 1st hour, but combined AOD and PM_{2.5} DA produced the lowest bias for all times. It is encouraging that assimilating only total AOD—a column-integrated quantity—can improve the bias of surface aerosols, and this finding is consistent with LIU11.

[75] Poor MODIS AOD data quality in the southwest CONUS degraded AOD and surface PM_{2.5} forecasts in that region when AOD was assimilated, while PM_{2.5} DA had a neutral effect. Elsewhere, aerosol DA improved forecasts, particularly in the central and eastern CONUS and southern Canada. Assimilating just surface PM_{2.5} observations did not improve AOD forecasts compared to the control, but AOD DA, either by itself or in conjunction with PM_{2.5} DA, produced the best AOD forecasts. Additionally, all forms of DA unequivocally improved surface PM_{2.5} forecasts through at least ~30 h. Through ~15–18 h, PM_{2.5} forecasts were better when assimilating just PM_{2.5} rather than solely AOD, although, for longer forecasts, assimilating only AOD yielded comparable or slightly better PM_{2.5} forecasts than just assimilating PM_{2.5}. However, the best PM_{2.5} forecasts were achieved when MODIS AOD and AIRNow PM_{2.5} observations were assimilated concurrently.

[76] Considering the goodness of both AOD and PM_{2.5} forecasts, the combination of AOD and PM_{2.5} DA clearly produced superior aerosol predictions. The informational content of both observation types was optimally combined within a common variational framework, leading to analyses that reflected the contributions of both individual sources. These results indicate that both AOD and surface PM_{2.5} observations should be assimilated if the observations are available, as the different observations work synergistically.

[77] While 3DVAR is computationally efficient and easily permits multiple species in the analysis vector, its main limitation is the static BECs. More advanced DA techniques, such as EnDA, may be superior to 3DVAR by calculating multivariate and flow-dependent BECs that better represent “errors of the day.” However, EnDA approaches are more computationally expensive and perhaps impractical for

operational applications when the number of control variables grows too large.

[78] Finally, the aerosol DA system developed by LIU11 and used again here can be continually extended to assimilate additional aerosol-related observations. Given these results, future efforts should continue to focus on assimilating aerosol observations from disparate observing platforms. Assimilating more observations from different sources and wavelengths should refine vertical structures of aerosol mass and better quantify individual species' contributions to total aerosol mass. Additionally, speciated aerosol measurements (e.g., BC, OC) can be assimilated easily in this system and should improve forecasts of individual species. However, these advancements rely on the availability of suitable aerosol data, which underscores the need for additional aerosol observing networks, particularly those that provide vertical information about aerosol mass.

[79] **Acknowledgments.** We are grateful to the Air Force Weather Agency for funding this work. AERONET Principal Investigators are also thanked for making their data available. Georg Grell, Steven Peckham, and Mariusz Pagowski (NOAA) provided valuable assistance regarding WRF-Chem configurations. Comments from three anonymous reviewers improved the quality of this manuscript. NCAR is sponsored by the National Science Foundation.

References

- Adhikary, B., S. Kulkarni, A. D'allura, Y. Tang, T. Chai, L. R. Leung, Y. Qian, C. E. Chung, V. Ramanathan, and G. R. Carmichael (2008), A regional scale chemical transport modeling of Asian aerosols with data assimilation of AOD observations using optimal interpolation technique, *Atmos. Environ.*, *42*(37), 8600–8615, doi:10.1016/j.atmosenv.2008.08.031.
- Amiridis, V., D. Balis, S. Kazadzis, A. Bais, E. Giannakaki, A. Papayannis, and C. Zerefos (2005), Four years aerosol observations with a Raman lidar at Thessaloniki, Greece in the framework of EARLINET, *J. Geophys. Res.*, *110*, D21203, doi:10.1029/2005JD006190.
- Benedetti, A., et al. (2009), Aerosol analysis and forecast in the European Centre for Medium-Range Weather Forecasts Integrated Forecast System: 2. Data assimilation, *J. Geophys. Res.*, *114*, D13205, doi:10.1029/2008JD011115.
- Chin, M., R. B. Rood, S.-J. Lin, J.-F. Muller, and A. M. Thompson (2000), Atmospheric sulfur cycle simulated in the global model GOCART: Model description and global properties, *J. Geophys. Res.*, *105*, 24,671–24,687, doi:10.1029/2000JD900384.
- Chin, M., P. Ginoux, S. Kinne, O. Torres, B. N. Holben, B. N. Duncan, R. V. Martin, J. A. Logan, and A. Higurashi (2002), Tropospheric aerosol optical thickness from the GOCART model and comparisons with satellite and Sun photometer measurements, *J. Atmos. Sci.*, *59*, 461–483, doi:10.1175/1520-0469(2002)059<0461:TAOTFT>2.0.CO;2.
- Collins, W. D., P. J. Rasch, B. E. Eaton, B. V. Khattatov, and J.-F. Lamarque (2001), Simulating aerosols using a chemical transport model with assimilation of satellite aerosol retrievals: Methodology for INDOEX, *J. Geophys. Res.*, *106*, 7313–7336, doi:10.1029/2000JD900507.
- Drury, E., D. J. Jacob, J. Wang, R. J. D. Spurr, and K. Chance (2008), Improved algorithm for MODIS satellite retrievals of aerosol optical depths over western North America, *J. Geophys. Res.*, *113*, D16204, doi:10.1029/2007JD009573.
- Drury, E., D. J. Jacob, R. J. D. Spurr, J. Wang, Y. Shinzuka, B. E. Anderson, A. D. Clarke, J. Dibb, C. McNaughton, and R. Weber (2010), Synthesis of satellite (MODIS), aircraft (ICARTT), and surface (IMPROVE, EPA-AQS, AERONET) aerosol observations over eastern North America to improve MODIS aerosol retrievals and constrain surface aerosol concentrations and sources, *J. Geophys. Res.*, *115*, D14204, doi:10.1029/2009JD012629.
- Elbern, H., A. Strunk, H. Schmidt, and O. Talagrand (2007), Emission rate and chemical state estimation by 4-dimensional variational inversion, *Atmos. Chem. Phys.*, *7*, 3749–3769, doi:10.5194/acp-7-3749-2007.
- Engel-Cox, J. A., C. H. Holloman, B. W. Coutant, and R. M. Hoff (2004), Qualitative and quantitative evaluation of MODIS satellite sensor data for regional and urban scale air quality, *Atmos. Environ.*, *38*, 2495–2509, doi:10.1016/j.atmosenv.2004.01.039.
- Evensen, G. (1994), Sequential data assimilation with a nonlinear quasi-geostrophic model using Monte Carlo methods to forecast error statistics, *J. Geophys. Res.*, *99*, 10,143–10,162, doi:10.1029/94JC00572.
- Forster, P. et al. (2007), Changes in atmospheric constituents and in radiative forcing, in *Climate Change 2007: The Physical Science Basis. Contribution of Working Group I to the Fourth Assessment Report of the Intergovernmental Panel on Climate Change*, edited by S. Solomon et al., pp. 129–234, Cambridge Univ. Press, Cambridge, U. K.
- Gauthier, P., M. Tanguay, S. Laroche, S. Pellerin, and J. Morneau (2007), Extension of 3DVAR to 4DVAR: Implementation of 4DVAR at the Meteorological Service of Canada, *Mon. Weather Rev.*, *135*, 2339–2354, doi:10.1175/MWR3394.1.
- Generoso, S., F.-M. Bréon, F. Chevallier, Y. Balkanski, M. Schulz, and I. Bey (2007), Assimilation of POLDER aerosol optical thickness into the LMDz-INCA model: Implications for the Arctic aerosol burden, *J. Geophys. Res.*, *112*, D02311, doi:10.1029/2005JD006954.
- Ginoux, P., M. Chin, I. Tegen, J. Prospero, B. Holben, O. Dubovik, and S.-J. Lin (2001), Sources and distributions of dust aerosols simulated with the GOCART model, *J. Geophys. Res.*, *106*, 20,255–20,273, doi:10.1029/2000JD000053.
- Grell, G. A., S. E. Peckham, R. Schmitz, S. A. McKeen, G. Frost, W. C. Skamarock, and B. Eder (2005), Fully coupled “online” chemistry within the WRF model, *Atmos. Environ.*, *39*, 6957–6975, doi:10.1016/j.atmosenv.2005.04.027.
- Han, Y., P. van Delst, Q. Liu, F. Weng, B. Yan, R. Treadon, and J. Derber (2006), JCSDA Community Radiative Transfer Model (CRTM)—Version 1, *NOAA Tech. Rep. NESDIS 122*, 33 pp., NOAA, Silver Spring, Md.
- Holben, B. N., et al. (1998), AERONET—A federated instrument network and data archive for aerosol characterization, *Remote Sens. Environ.*, *66*, 1–16, doi:10.1016/S0034-4257(98)00031-5.
- Huang, X.-Y., et al. (2009), Four-dimensional variational data assimilation for WRF: Formulation and preliminary results, *Mon. Weather Rev.*, *137*, 299–314, doi:10.1175/2008MWR2577.1.
- Kahnert, M. (2008), Variational data analysis of aerosol species in a regional CTM: Background error covariance constraint and aerosol optical observation operators, *Tellus, Ser. B*, *60*, 753–770, doi:10.1111/j.1600-0889.2008.00377.
- Kim, S.-W., et al. (2011), Evaluations of NO_x and highly reactive VOC emission inventories in Texas and their implications for ozone plume simulations during the Texas Air Quality Study 2006, *Atmos. Chem. Phys.*, *11*, 11,361–11,386, doi:10.5194/acp-11-11361-2011.
- Kleist, D. T., D. F. Parrish, J. C. Derber, R. Treadon, W.-S. Wu, and S. Lord (2009), Introduction of the GSI into the NCEP Global Data Assimilation System, *Weather Forecast.*, *24*, 1691–1705, doi:10.1175/2009WAF2222201.1.
- Lean, H. W., P. A. Clark, M. Dixon, N. M. Roberts, A. Fitch, R. Forbes, and C. Halliwell (2008), Characteristics of high-resolution versions of the Met Office Unified Model for forecasting convection over the United Kingdom, *Mon. Weather Rev.*, *136*, 3408–3424, doi:10.1175/2008MWR2332.1.
- Lin, C., Z. Wang, and J. Zhu (2008), An ensemble Kalman filter for severe dust storm data assimilation over China, *Atmos. Chem. Phys.*, *8*, 2975–2983, doi:10.5194/acp-8-2975-2008.
- Liu, Q., and F. Weng (2006), Advanced doubling-adding method for radiative transfer in planetary atmosphere, *J. Atmos. Sci.*, *63*(12), 3459–3465, doi:10.1175/JAS3808.1.
- Liu, Z., and F. Rabier (2002), The interaction between model resolution, observation resolution and observation density in data assimilation: A one-dimensional study, *Q. J. R. Meteorol. Soc.*, *128*, 1367–1386, doi:10.1256/003590002320373337.
- Liu, Z., Q. Liu, H.-C. Lin, C. S. Schwartz, Y.-H. Lee, and T. Wang (2011), Three-dimensional variational assimilation of MODIS aerosol optical depth: Implementation and application to a dust storm over East Asia, *J. Geophys. Res.*, *116*, D23206, doi:10.1029/2011JD016159.
- Lorenc, A. C. (1981), A global 3D multivariate statistical interpolation scheme, *Mon. Weather Rev.*, *109*, 701–721, doi:10.1175/1520-0493(1981)109<0701:AGTDM>2.0.CO;2.
- Lorenc, A. C. (1986), Analysis method for numerical weather prediction, *Q. J. R. Meteorol. Soc.*, *112*, 1177–1194, doi:10.1002/qj.49711247414.
- Lorenc, A. C., et al. (2000), The Met Office global 3-dimensional variational data assimilation scheme, *Q. J. R. Meteorol. Soc.*, *126*, 2991–3012, doi:10.1002/qj.49712657002.
- McKeen, S., et al. (2009), An evaluation of real-time air quality forecasts and their urban emissions over eastern Texas during the summer of 2006 Second Texas Air Quality Study field study, *J. Geophys. Res.*, *114*, D00F11, doi:10.1029/2008JD011697.
- Mittermaier, M., and N. Roberts (2010), Intercomparison of spatial forecast verification methods: Identifying skillful spatial scales using the

- fractions skill score, *Weather Forecast.*, 25, 343–354, doi:10.1175/2009WAF2222260.1.
- Niu, T., S. L. Gong, G. F. Zhu, H. L. Liu, X. Q. Hu, C. H. Zhou, and Y. Q. Wang (2008), Data assimilation of dust aerosol observations for the CUACE/dust forecasting system, *Atmos. Chem. Phys.*, 8, 3473–3482, doi:10.5194/acp-8-3473-2008.
- Pagowski, M., G. A. Grell, S. A. McKeen, S. E. Peckham, and D. Devenyi (2010), Three-dimensional variational data assimilation of ozone and fine particulate matter observations: Some results using the Weather Research and Forecasting–Chemistry model and grid-point statistical interpolation, *Q. J. R. Meteorol. Soc.*, 136, 2013–2024, doi:10.1002/qj.700.
- Parrish, D. F., and J. C. Derber (1992), The National Meteorological Center's spectral statistical interpolation analysis system, *Weather Rev.*, 120, 1747–1763, doi:10.1175/1520-0493(1992)120<1747:TNMCSS>2.0.CO;2.
- Pope, C. A., R. T. Burnett, M. J. Thun, E. E. Calle, D. Krewski, K. Ito, and G. D. Thurston (2002), Lung cancer, cardiopulmonary mortality, and long-term exposure to fine particulate air pollution, *J. Am. Med. Assoc.*, 287(9), 1132–1141, doi:10.1001/jama.287.9.1132.
- Prados, A. I., S. Kondragunta, P. Ciren, and K. R. Knapp (2007), GOES Aerosol/Smoke Product (GASP) over North America: Comparisons to AERONET and MODIS observations, *J. Geophys. Res.*, 112, D15201, doi:10.1029/2006JD007968.
- Rabier, F., A. McNally, E. Andersson, P. Courtier, P. Undén, J. Eyre, A. Hollingsworth, and F. Bouët (1998), The ECMWF implementation of three-dimensional variational assimilation (3D-Var). II: Structure functions, *Q. J. R. Meteorol. Soc.*, 124, 1809–1829, doi:10.1002/qj.49712455003.
- Rabier, F., H. Jarvinen, E. Klinker, J.-F. Mahfouf, and A. Simmons (2000), The ECMWF operational implementation of four-dimensional variational assimilation. I: Experimental results with simplified physics, *Q. J. R. Meteorol. Soc.*, 126, 1143–1170, doi:10.1256/smsqj.56414.
- Remer, L. A., et al. (2005), The MODIS aerosol algorithm, products, and validation, *J. Atmos. Sci.*, 62, 947–973, doi:10.1175/JAS3385.1.
- Roberts, N. M., and H. W. Lean (2008), Scale-selective verification of rainfall accumulations from high-resolution forecasts of convective events, *Mon. Weather Rev.*, 136, 78–97, doi:10.1175/2007MWR2123.1.
- Rodwell, M. (2005), The local and global impact of the recent change in aerosol climatology, *ECMWF Newsl.*, 105, 17–23.
- Rogers, E., et al. (2009), The NCEP North American mesoscale modeling system: Recent changes and future plans. Paper presented at 23rd Conference on Weather Analysis and Forecasting, Am. Meteorol. Soc., Boston, Mass. [Available at <http://ams.confex.com/ams/pdfpapers/154114.pdf>.]
- Schroedter-Homscheidt, M., H. Elbern, and T. Holzer-Popp (2010), Observation operator for the assimilation of aerosol type resolving satellite measurements into a chemical transport model, *Atmos. Chem. Phys.*, 10, 10,435–10,452, doi:10.5194/acp-10-10435-2010.
- Schutgens, N. A. J., T. Miyoshi, T. Takemura, and T. Nakajima (2010), Applying an ensemble Kalman filter to the assimilation of AERONET observations in a global aerosol transport model, *Atmos. Chem. Phys.*, 10, 2561–2576, doi:10.5194/acp-10-2561-2010.
- Schwartz, C. S., et al. (2009), Next-day convection-allowing WRF model guidance: A second look at 2-km versus 4-km grid spacing, *Mon. Weather Rev.*, 137, 3351–3372, doi:10.1175/2009MWR2924.1.
- Sekiyama, T. T., T. Y. Tanaka, A. Shimizu, and T. Miyoshi (2010), Data assimilation of CALIPSO aerosol observations, *Atmos. Chem. Phys.*, 10, 39–49, doi:10.5194/acp-10-39-2010.
- Sekiyama, T. T., T. Y. Tanaka, T. Maki, and M. Mikami (2011), The effects of snow cover and soil moisture on Asian dust: II. Emission estimation by Lidar data assimilation, *SOLA*, 7A, 40–43, doi:10.2151/sola.7A-011.
- Skamarock, W. C., J. B. Klemp, J. Dudhia, D. O. Gill, D. M. Barker, M. G. Duda, X.-Y. Huang, W. Wang, and J. G. Powers (2008), A description of the Advanced Research WRF version 3, *NCAR Tech Note NCAR/TN-475+STR*, 113 pp. NOAA, Boulder, Colo.
- Stockwell, W. R., F. Kirchner, M. Kuhn, and S. Seefeld (1997), A new mechanism for regional atmospheric chemistry modeling, *J. Geophys. Res.*, 102(D22), 25,847–25,879, doi:10.1029/97JD00849.
- Tombette, M., V. Mallet, and B. Sportisse (2009), PM₁₀ data assimilation over Europe with the optimal interpolation method, *Atmos. Chem. Phys.*, 9, 57–70, doi:10.5194/acp-9-57-2009.
- U.S. Environmental Protection Agency (2010), Preparation of emissions inventories for the version 4, 2005-based platform, technical support document, 73 pp., Off. of Air Qual. Plann. and Stand., EPA, Washington, D. C. [Available at http://www.epa.gov/airquality/transport/pdfs/2005_emissions_tsd_07jul2010.pdf.]
- van de Hulst, H. C. (1957), *Light Scattering by Small Particles*, 470 pp., John Wiley, Hoboken, N. J.
- Volkamer, R., J. L. Jimenez, F. S. Martini, K. Dzepina, Q. Zhang, D. Salcedo, L. T. Molina, D. R. Worsnop, and M. J. Molina (2006), Secondary organic aerosol formation from anthropogenic air pollution: Rapid and higher than expected, *Geophys. Res. Lett.*, 33, L17811, doi:10.1029/2006GL026899.
- Wang, J., U. S. Nair, and S. A. Christopher (2004), GOES 8 aerosol optical thickness assimilation in a mesoscale model: Online integration of aerosol radiative effects, *J. Geophys. Res.*, 109, D23203, doi:10.1029/2004JD004827.
- Welton, E. J., and J. R. Campbell (2002), Micro-pulse Lidar signals: Uncertainty analysis, *J. Atmos. Oceanic Technol.*, 19, 2089–2094, doi:10.1175/1520-0426(2002)019<2089:MLSUA>2.0.CO;2.
- Winker, D. M., M. A. Vaughan, A. Omar, Y. Hu, K. A. Powell, Z. Liu, W. H. Hunt, and S. A. Young (2009), Overview of the CALIPSO mission and CALIOP data processing algorithms, *J. Atmos. Oceanic Technol.*, 26, 2310–2323, doi:10.1175/2009JTECHA1281.1.
- Wu, W.-S., D. F. Parrish, and R. J. Purser (2002), Three-dimensional variational analysis with spatially inhomogeneous covariances, *Mon. Weather Rev.*, 130, 2905–2916, doi:10.1175/1520-0493(2002)130<2905:TDAVWS>2.0.CO;2.
- Yu, H., R. E. Dickinson, M. Chin, Y. J. Kaufman, B. Geogdzhayev, and M. I. Mishchenko (2003), Annual cycle of global distributions of aerosol optical depth from integration of MODIS retrievals and GOCART model simulations, *J. Geophys. Res.*, 108(D3), 4128, doi:10.1029/2002JD002717.
- Zhang, J., and J. S. Reid (2006), MODIS aerosol product analysis for data assimilation: Assessment of over-ocean level 2 aerosol optical thickness retrievals, *J. Geophys. Res.*, 111, D22207, doi:10.1029/2005JD006898.
- Zhang, J., J. S. Reid, and B. N. Holben (2005), An analysis of potential cloud artifacts in MODIS over ocean aerosol optical thickness products, *Geophys. Res. Lett.*, 32, L15803, doi:10.1029/2005GL023254.
- Zhang, J., J. S. Reid, D. Westphal, N. Baker, and E. Hyer (2008), A system for operational aerosol optical depth data assimilation over global oceans, *J. Geophys. Res.*, 113, D10208, doi:10.1029/2007JD009065.
- Zhang, Q., et al. (2007), Ubiquity and dominance of oxygenated species in organic aerosols in anthropogenically influenced Northern Hemisphere midlatitudes, *Geophys. Res. Lett.*, 34, L13801, doi:10.1029/2007GL029979.